

Unveiling the decomposing and mineralizing mechanism of novel perfluoroalkyl acids via hydroxyl radical dominated electrochemical oxidation

Meng Li ^{a,b,c}, Hongguo Zhang ^a, Jiliang Cheng ^b, Jiayu Song ^c, Wei Han ^d, Shaoqi Zhou ^{e,*}, Zhao-Xin Zhang ^f, Qiong Wu ^{c,d,**}, King Lun Yeung ^{c,d}, Ce-Hui Mo ^{b,*}

^a School of Environmental Science and Engineering, Guangzhou University, Guangzhou, 510006, PR China

^b Guangdong Provincial Research Center for Environment Pollution Control and Remediation Materials, College of Life Science and Technology, Jinan University, Guangzhou 510632, PR China

^c Department of Chemical and Biological Engineering, The Hong Kong University of Science and Technology, Clear Water Bay, Kowloon, Hong Kong Special Administrative Region of China

^d Division of Environment and Sustainability, Hong Kong University of Science and Technology, Clear Water Bay, Kowloon, Hong Kong Special Administrative Region of China

^e College of Resources and Environmental Engineering, Guizhou University, 2708 Huaxi Road, Guiyang 550025, PR China

^f Division of Emerging Interdisciplinary Areas, The Hong Kong University of Science and Technology, Clear Water Bay, Kowloon, Hong Kong Special Administrative Region of China



ARTICLE INFO

Keywords:

Emerging organic pollutants
Hydroxyl radical
Catalytic oxidation
Reaction mechanism

ABSTRACT

A cerium-doped Sb₂S₃ anode is successfully fabricated for perfluoroalkyl acids (PFAAs) degradation via a hydroxyl radical dominant electrochemical oxidation (EO) coupled peroxyomonosulfate (PMS) reaction. Various PFAAs can be efficiently removed within 25 min with high mineralization and low energy consumption. The hydroxyl radical, sulfate radical, and electron transfer are responsible for PFAAs degradation, and the hydroxyl radical played a dominant role. The electron can be moved from the highest occupied molecular orbital of these PFAAs to the lowest unoccupied molecular orbital of PMS via potential energy difference, further decomposing PMS to generate hydroxyl and sulfate radical for PFAAs degradation. Besides, the corresponding degradation pathway, defluorination, and Gibbs free energy of the reaction for each PFAAs were elucidated based on the identified intermediates and density functional theory calculations. The current study provides insight into the efficient decomposition mechanism of various PFAAs during EO and highlights its promising potential in environmental remediation.

1. Introduction

Since the 1900 s, per- and poly-fluoroalkyl substances (PFAS) have been extensively used in industrial applications and various consumer products such as leather, cement, floor polishes, metal cleaners, and foam-based fire extinguishers owing to their physicochemical properties and thermal degradation [1,2]. PFAS contaminants have gained public concern because they possess extreme chemical stability, widespread occurrence, significant bioaccumulation potential, and are toxic to humans and wildlife. Various efforts have been made to reduce their use

and production [3,4]. The most recalcitrant substance among PFAS with an extreme persistence, Perfluoroalkyl acids (PFAAs) are considered “forever chemicals” owing to the presence of a polarity tail and high energy carbon–fluorine bond (116 kcal mol⁻¹) in their molecular framework [5]. Once in contact with the environment, PFAAs are challenging to degrade and can remain and migrate worldwide for hundreds of years [6]. Among these PFAAs, short-chain perfluorobutyric acid (PFBA), perfluorobutane sulfonate (PFBS), long-chain perfluorooctanoic acid (PFOA), and perfluorooctane sulfonate (PFOS) have significant applications and gained attention [6]. Recently,

* Corresponding authors.

** Corresponding author at: Department of Chemical and Biological Engineering, The Hong Kong University of Science and Technology, Clear Water Bay, Kowloon, Hong Kong Special Administrative Region of China.

E-mail addresses: zhousq@gzu.edu.cn (S. Zhou), kekyeung@ust.hk (K.L. Yeung), tchmo@jnu.edu.cn (C.-H. Mo).

high-mobility PFOS have been reported in water environments ranging from dozens of pg L^{-1} to dozens of $\mu\text{g L}^{-1}$, and even reaching mg L^{-1} level in the polluted areas, which significantly exceeds the safety standard (70 ng L^{-1}) proposed by the United States Environment Protection Agency [7]. In addition, PFOS has been included in the list of persistent organic pollutants by the Stockholm Convention in 2009 [8]. If these PFAAs have not been handled properly, they will accumulate in animal and human muscles, causing a series of diseases, such as liver damage, carcinogenicity, thyroid disease, mutagenicity, high cholesterol, and immunotoxicity [1,9,10]. The continuous release of PFAAs into the environment has led to public exposure to PFAAs via the consumption of contaminated food, dust inhalation, and drinking water [2,11]. Consequently, it is urgent to develop effective technologies to remediate PFAAs.

Various approaches have been developed to remove PFAAs from aqueous solutions, such as adsorption [12], reverse osmosis [13], coagulation [14], ultrasonic irradiation [15], the electron beam [16], thermal treatment [17], photocatalysis [18], and advanced oxidation process (AOP) [19]. However, methods involving adsorption, reverse osmosis, and coagulation cannot degrade PFAAs and only convert liquid PFAAs into their solid state, resulting in a secondary pollutant. In addition, ultrasonic irradiation, electron beam, thermal treatment, and photocatalysis require harsh reaction conditions or specific equipment [20]. Although AOP as a promising wastewater treatment technology, can generate active oxidizing agents such as hydroxyl ($\bullet\text{OH}$) and sulfate free radicals ($\text{SO}_4^{\bullet-}$) at room temperature for the treatment of various wastewater (oily wastewaters, landfill leachate, denitrification with Fenton oxidized non-degradable large molecular organic pollutants, and removal of phosphorus, etc.) [21,22], $\bullet\text{OH}$ and $\text{SO}_4^{\bullet-}$ cannot still rapidly and effectively degrade PFAAs due to the stable carbon-chains with fluorine atom [19]. Some studies have confirmed that electrochemical oxidation (EO) can effectively mineralize PFAAs because it is an efficient, safe, environmental-friendly, and mild processing technique to degrade PFAAs from wastewater consuming lower electrical energy than those of other AOP methods [4,23]. In addition, EO is more potent than the traditional AOP because EO combines the direct electron transfer (DET) actions on the anode surface [24]. Furthermore, EO uses an electrode that can achieve high anodic potential, which is necessary to determine the rate-limiting step with a DET reaction [25]. During EO, the organic pollutant removal rate directly relates to the ability of reactive oxygen species (ROS) containing $\text{SO}_4^{\bullet-}$, $\bullet\text{OH}$, and $\text{O}_2^{\bullet-}$, the conductivity of the electrode, and the electron transfer efficiency between the electrode and the electrolyte [26]. The traditional anode materials, such as boron-doped diamond (BDD) [27], graphite-based materials (graphite rod, plate, and felt) [28,29], precious metals [29], and three-dimensional materials (PbO_2 , SnO_2 , IrO_2 , and RuO_2) have been applied to remove various organic pollutants [30,31]. The BDD electrode has been selected for the electrochemical degradation of PFAAs owing to the advantages of high oxygen evolution potential, long lifetime, and good chemical and electrochemical stability [27]. However, the production cost of BDD electrodes is very expensive and demanding to prepare on a large scale [32]. In addition, it is challenging to discover a suitable substrate to deposit the diamond layer. Furthermore, the conventional three-dimensional electrodes are not ideal for scale-up applications due to their relatively slow reaction rate and the metal ion leaching during EO [33,34]. Consequently, developing highly efficient, safe, and cost-effective electrodes is essential to address the abovementioned issues for removing PFAAs via EO.

Titanium (Ti) plate has been extensively applied as a carrier of the electrode or supercapacitor in electrochemical field owing to its high specific strength and excellent corrosion resistance. Zeng et al. fabricated a Ti-based Sb/ SnO_2 membrane that could effectively degrade sulfamethoxazole and achieve a high removal rate of 92.6% [35]. Sun et al. discovered that a Ti-based Sn–Sb/ $\gamma\text{-Al}_2\text{O}_3$ electrode with excellent electrocatalytic ability showed a strong oxidizing capacity to degrade oxytetracycline and achieved a removal efficiency of 95.7% [36]. Man

et al. incorporated Ce and Sb into SnO_2 to form Ti/Ce–Sb– SnO_2 -nano-flower electrodes for electrochemically degrading organic pollutants. This electrode achieved ~100% decolorization efficiency and 91.5% mineralization efficiency of methylene blue [37]. The above studies confirmed that adding Ce or Sb could significantly improve the performance of the electrode. Among numerous inorganic metal compounds, Sb_2S_3 nanostructures have been widely used as counter electrodes in electrochemical reactions, which confirmed their high oxidation resistance and strong conductivity [38]. A previous study confirmed, as an anode material, Sb_2S_3 exhibited excellent electrochemical properties (high theoretical capacity of 946 mAh g^{-1}), which was larger than those of Sb or Sb-based materials due to their multi-electron reactions in the electrochemical process [39]. In addition, Sb_2S_3 nanostructures consisted of short and strong Sb–S covalent bonds, accompanied by a relatively small volume change, which is beneficial for electrochemical reactions on the electrode [39,40]. To further promote the electrocatalytic activity and lifespan of the Sb_2S_3 electrode, Ce was doped to regulate the Sb_2S_3 active layer to disperse internal stress and enhance the binding force between the electrode and active layer [37,41]. Based on these results, a Ce-doped Sb_2S_3 (Ce/ Sb_2S_3) electrode was fabricated for the degradation of PFAAs in our study.

Although EOs degrade PFAAs, most EOs have mainly concentrated on degrading a single organic PFAAs, [42,43] and the degradation of short- and long-chain PFAAs still needs to be clarified. In addition, oxidation in a water environment is based on $\bullet\text{OH}$ radical, but the complex water matrices containing radical scavengers might limit the EO efficiency owing to the short half-life of $\bullet\text{OH}$ radical ($t_{1/2} = 20 \text{ ns}$) [44]. Recently, many studies have employed reactive substances with a long half-life and high selectivity to degrade organic pollutants. For example, peroxyomonosulfate (PMS) is selected as an effective oxidant owing to its asymmetric structure and long half-life ($t_{1/2} = 30\text{--}40 \mu\text{s}$). The final product required for PMS activation is $\text{SO}_4^{\bullet-}$, which is harmless in water environment [44]. In addition, to the best of our knowledge, it is the first time to explore PFAAs degradation via EO by PMS activation using Ce/ Sb_2S_3 electrode. Many studies have been devoted to exploring the degradation and removal of PFAAs with various techniques. Still, some key points are neglected, such as (i) the degree of contribution of each active species for the PFAAs degradation, (ii) the relationship between molecular orbital energy and kinetic rate, (iii) the pathway of electron transfer during electrochemical reaction, (iv) the mechanism of defluorination, (v) the formation mechanism of PFAA radical and carbon-fluorine radicals, (vi) the key reaction site for the degradation of PFAAs, and (vii) the degradation pathways of various PFAAs.

To address the issues mentioned above, short-chains of PFBA and PFBS and long-chains of PFOA and PFOS were selected as model contaminants, and their degradation in an aqueous solution was explored by EO using Ce/ Sb_2S_3 electrode and PMS activation. In the present study, the impact of different electrodes, initial PMS concentration, and input current density on the efficiency of PFAAs, total organic carbon (TOC), and electrical energy consumption of EO was explored. In addition, the key ROS and the corresponding contribution to the PFAAs degradation were determined by free radical quenching experiments and electron paramagnetic resonance (EPR) spectroscopy. The key reaction sites of PMS on the electrode surface, the corresponding adsorption energy, the free radical generation pathways, the relationship between molecular orbital energy difference and kinetic rate constant, and the related electron transfer pathway in degrading PFAAs were investigated by performing density functional theory (DFT). Moreover, the electrostatic potential (ESP), the molecular charge of different PFAAs, and the reaction-free energy changes were conducted by quantum chemical calculations to accurately estimate the key attacking sites for the PFAAs degradation, confirming the PFAAs degradation pathways. The fluorine balance for the degradation of different PFAAs was also studied to prove defluorination in degrading PFAAs via EO. The stability and applied potential of EO for PFAAs degradation were validated based on the impacts of different water matrices, recycling experiments, and surface

characterizations. The comprehensive explorations of this study were to achieve a deeper understanding of the mechanism of PFAAs degradation and provide insights into the promising use of EO with a Ce/Sb₂S₃ electrode for the treatment of persistent organic pollutants and environmental remediation.

2. Methods and methods

2.1. Chemicals

PFOA, PFOS, PFBA, PFBS, and mass-labeled PFAA injection standard solutions (¹⁴C₃-PFAAs) were obtained from the Wellington laboratory (Ontario, Canada). Oxone (KHSO₅·0.5KHSO₄·0.5 K₂SO₄, PMS), sodium sulfate (Na₂SO₄), methanol (MeOH), tert-butanol (TBA), hexane, isopropyl alcohol, p-benzoquinone (BQ), L-histidine (LH), sodium azide (NaN₃), nitrobenzene (NB), atrazine (ATZ) cerium acetate, sulfur, oleylamine, paraffin oil, ethyl hexanoic acid, 5,5-dimethyl-1-pyrroline-N-oxide (DMPO), antimony trichloride (SbCl₃) were purchased from Sigma-Aldrich. 2,2,6,6-tetramethylpiperidine (TEMP) was from Dayang Chem, Hangzhou, China. Nafion solution was purchased from Shanghai Hesen Electric Co., Ltd. The Ti plate was obtained from Baoji Zhongtai Metal Material Co., Ltd.

2.2. Fabrication of electrodes

First, 1.0 mM elemental sulfur was dissolved in 6 mL oleylamine by sonification for 30 min (S precursor). Second, 20 mL of paraffin oil was added to the above solution, and then the solution mixture was heated to 150 °C for 1 h. Next, 2 mM SbCl₃ was added to 10 mL of ethyl hexanoic acid at a temperature of 100 °C for 1 h (Sb precursor). Then, the Sb precursor was slowly added into the S precursor to form a solution mixture, and then the solution was heated to 230 °C for 20 min and mixed by magnetic stirring (1000 rpm). After the above mixture solution cooling down using an ice bath, 10 mL of hexane and 20 mL of isopropyl alcohol were added to the solution to precipitate. Subsequently, the precipitation was dispersed in chlorobenzene solution, and 10 μL Nafion solution (5%) were added into the above solution to form a sol-gel. Next, the solution was coated on both sides of the Ti plate (3 × 3 cm). That Ti plate was vacuum-dried in an oven at 60 °C for 1 h and was moved to a tubular furnace with the protection of N₂ purging at 500 °C for 30 min. The coating process were repeated ten times, and the final electrode was defined as Sb₂S₃/Ti. For the fabrication of a Ce-doped Sb₂S₃ electrode (defined as Ce/Sb₂S₃), a similar preparation process to the synthesis of Sb₂S₃ was used, except that 10% of the precursor Sb was replaced with cerium acetate (0.2 mM).

2.3. Electrode construction and operation

PFAAs degradation was conducted in a reactor with an effective volume of 0.5 L. The fabricated electrode (Ce/Sb₂S₃) and Ti plate were used as anode and cathode, respectively. The optimal electrode gap was kept at 2 cm, and these electrodes were connected by a DC power source (HSPY-60-05, Beijing Hansheng Puyuan Ltd.) using wires. A magnetic stirring apparatus was used to ensure even mass transfer of the electrolyte with a stirring speed of 600 rpm. The electrolyte solution mainly contained PFAAs (10 mg L⁻¹), Na₂SO₄ solution (20 mM L⁻¹), and PMS solution (5 mM L⁻¹). The sample was extracted for each interval via a 0.2 μm filter membrane, and MeOH was added to the sample to quench active oxygen species. All the experimental processes were triplicated. The electrochemical measurements were operated in an electrochemical workstation (CorrTest, CS310) with three-electrode system.

2.4. Analytical methods

The concentration of PFAAs was determined by high-performance liquid chromatography-mass spectroscopy (HPLC-MS, Agilent 1290)

equipped with an API4000 Q-trap spectroscopy. The degradation intermediates of PFAAs were detected by HPLC-MS/MS (Agilent 1290-Qtrap, USA) with C18 column (BEH, 2.1 mm × 50 mm, 1.7 μm) at 40 °C using the mobile phase A (5 mM ammonium acetate in water) and B (5 mM ammonium acetate in methanol). The mobile phase was initially increased from 40% A to 90% A in 8 min and held for 4 min, followed by returning to 40% A in 5 min and kept at 40% for 3 min. The by-products were identified by electrospray negative ionization mass spectrometry with multiple reaction monitoring under the following conditions: the gas (N₂) pressure: 0.8 Mpa; the source temperature: 120 °C; the desolvation temperature: 320 °C; the capillary potential: 4.5 kV; the injection rate was 10 μL min⁻¹; the cone voltage -10 V. In addition, the full mass scan ranges were 50–213, 50–300, 50–414, and 50–500 for the degradation intermediates from PFBA, PFBS, PFOA, and PFOS, respectively. The mineralization degree of PFAAs via EO was determined by a total organic carbon analyzer (TOC-L-CPN, Shimadzu Co, Japan). The concentration of fluorine ions was detected via an ion chromatograph system (Dionex AS22, 50 × 4 mm). As trapping agents, DMPO and TEMP were added into the reaction system and were used to detect ROS via an EPR spectrum (Bruker USA).

The surface morphology of these electrodes was observed by scanning electron microscopy equipped with energy-dispersive X-ray spectroscopy (SEM-EDS, JSM-7610 F, Japan). The crystal structure and the elemental composition were analyzed using an X-ray diffractometer (XRD, Bruker, German) and X-ray photoelectron spectroscopy (XPS, Thermo scientific K-Alpha). The electrical energy consumption was evaluated by the EE/O value (kWh/m⁻³/order) based on the following equation (Eq. 1):

$$EE/O = \frac{U \times I \times t}{60V * \log(C_0/C_t)} \quad (1)$$

where U and I are the voltage (V) and current (A), respectively; t is the reaction time (min); V is the reactor volume (L); C₀ and C_t are the PFAAs concentrations at time of 0 and t, respectively.

The generated •OH radical during electro-activation of PMS can be measured by using NB as a probe because NB was an effective scavenger for •OH radical with high kinetic rate constant. The generated SO₄²⁻ radical can be measured by using ATZ as a probe because ATZ has high reaction rate constant with SO₄²⁻ radical. Thus, the steady-state concentration of •OH (Eqs. 2–3) and SO₄²⁻ (Eqs. 4–5) radicals during electro-activation of PMS were estimated based on the following equations [45, 46]:

$$\frac{d[NB]}{dt} = k_{NB,\cdot OH}[NB][\cdot OH] = k_{NB}[NB] \quad (2)$$

$$[\cdot OH] = \frac{k_{NB}}{k_{NB,\cdot OH}} \quad (3)$$

$$\frac{d[ATZ]}{dt} = k_{ATZ,\cdot OH}[ATZ][\cdot OH] + k_{ATZ,SO_4^{2-}}[ATZ][SO_4^{2-}] = k_{ATZ}[ATZ] \quad (4)$$

$$[SO_4^{2-}] = \frac{k_{ATZ} - k_{ATZ,\cdot OH}[\cdot OH]}{k_{ATZ,SO_4^{2-}}} \quad (5)$$

2.5. Quantum chemical simulations

The DFT calculations based on the adsorption energy were conducted using the DMol3 program package in Materials Studio based on the generalized gradient approximation (GGA) with the Predew-Bruke-Ernher functions [47,48]. The adsorption energy (E_a) of the PMS on the electrode surface was obtained from the following equation (Eq. 6):

$$E_a = E_{total} - E_{pms} - E_{surface}, \quad (6)$$

where E_{total} is the total adsorption energy of the PMS on the surface of the electrode, E_{pms} is the energy of the isolated monomer PMS, and E_{surface} is the energy of the isolated electrode surface.

The Fukui function and ESP were carried out using Gaussian 09 and GaussView 05 software with a basic set of ω B97XD/6-311 G(d)** [49, 50] and simultaneous add solvent model. The HOMO and LUMO of PFAAs were also calculated based the above software and the same basic set. The results were obtained by Multiwfn 3.7 software [51] and finally showed by VMD1.9.3 software [52]. In addition, the condensed Fukui index (f_a) on electrophilic attack was calculated based on the following equation (Eq. 7):

$$f_a^- = q_{N-1}^a - q q_N^a \quad (7)$$

where q^a is the atom charge of atom a and N is the charge quality number. In addition, the natural population analysis charge was used to analyze the reaction sites.

The electrostatic potential (ESP) value calculation contained four steps: GaussView 05 software was applied to draw the molecular structure of PFAAs, then optimized by Gaussian 09 with the basis set of ω B97XD/6-311 G**, and then calculated using Multiwfn 3.8 software, and finally showed by VMD1.9.4 software. The ESP value of PFAAs was further analyzed over different ESP ranges by Origin 9.8.0.200 software.

3. Results and discussion

3.1. Electrode characterization and oxidation of PFAAs

Fig. 1 shows the SEM micrographs of as-synthesized Sb_2S_3 and Ce- Sb_2S_3 electrodes. The pure Sb_2S_3 electrode (Fig. 1a) showed a band-shaped irregular structure. With the introduction of Ce into Sb_2S_3 , the band-shaped structure was covered with some nanoparticles (Fig. 1b–c). In addition, the size and shape of the Ce- Sb_2S_3 electrode were similar to those of the pure Sb_2S_3 electrode, whereas the band-shape structure in the Ce- Sb_2S_3 electrode was more regular and uniform than that of the Sb_2S_3 electrode. Further, the elemental mapping of the Ce- Sb_2S_3 electrode showed that Ce (Fig. 1d), Sb (Fig. 1e), and S (Fig. 1f) elements were uniformly distributed on the surface of the electrode, suggesting the successful introduction of Ce into Sb_2S_3 . The crystal structure of these electrodes was also explored through XRD, and the results are shown in Fig. 1g. The diffraction peaks of Sb_2S_3 and Ce- Sb_2S_3 electrodes were of orthorhombic stibnite structure and match well with the corresponding JCPDS card (PDF#42-1393) [53]. In addition, the diffraction peaks of Ce were observed in the spectra of the Ce- Sb_2S_3 electrode, further evidencing the effective synthesis of the Ce- Sb_2S_3 electrode. XPS was conducted to reveal detailed information on the elemental composition and chemical state of the as-synthesized sample. As presented in Fig. 1h, S 2p/s and Sb 3d peaks appeared on the XPS survey of the Sb_2S_3

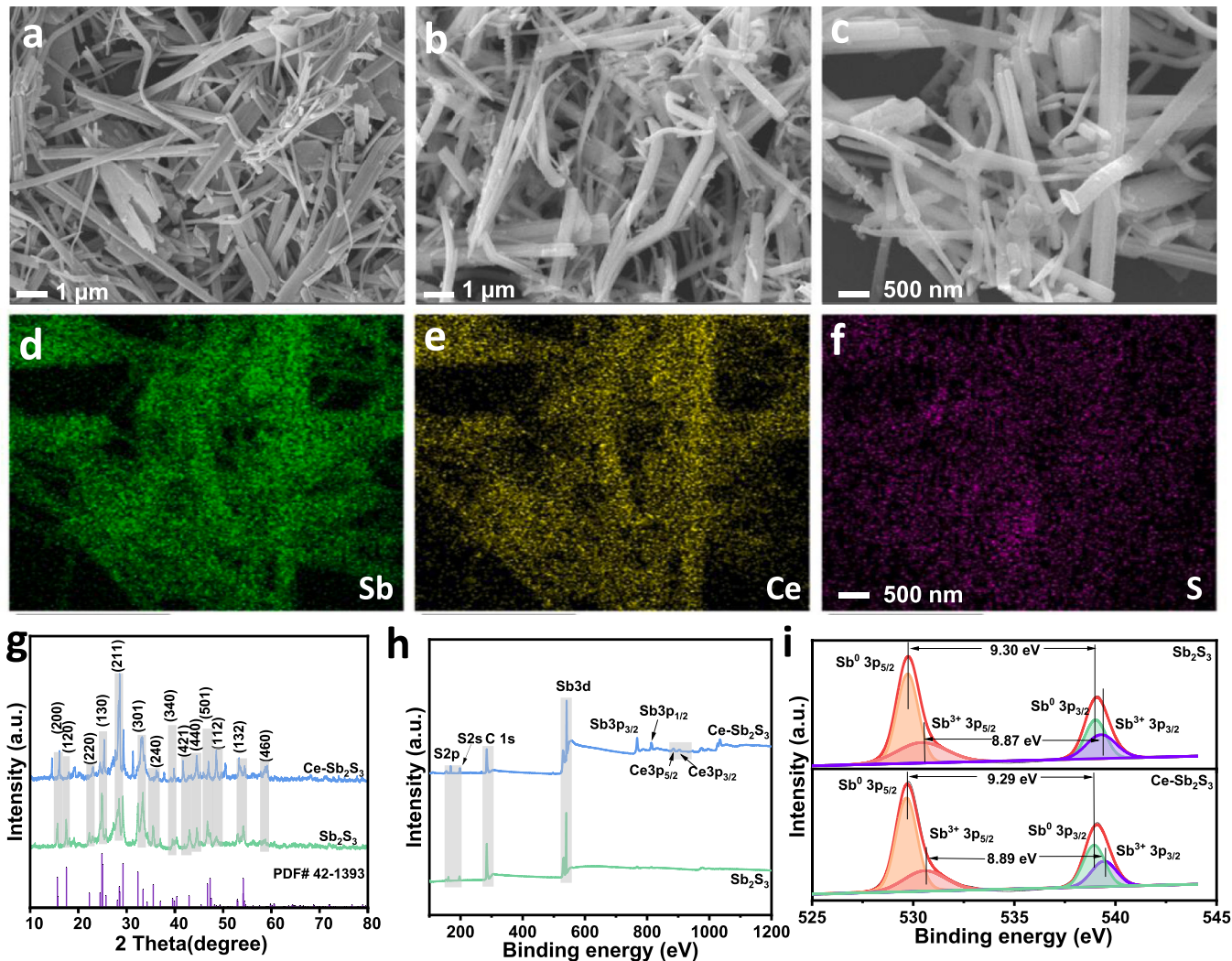


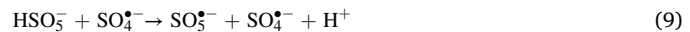
Fig. 1. Electrode characterization. Scanning electron microscopy micrographs of (a) Sb_2S_3 and (b–c) Ce- Sb_2S_3 electrodes. Elemental mapping images of the Ce- Sb_2S_3 electrode: (d) Sb, (e) Ce, and (f) S elements. (g) XRD pattern, (h) survey spectra, and (i) high-resolution Sb spectrum of the Ce- Sb_2S_3 electrode.

electrode while Ce 3p, S 2p/s, and Sb 3d peaks could be observed on the Ce–Sb₂S₃ electrode; this implies that Ce was successfully embedded after being modified. In addition, the high resolution of the Sb 3d XPS was observed in Fig. 1i. The binding energies at 529.70 and 530.45 eV corresponded to the peaks of Sb 3d_{5/2}, and the binding energies at 539.0 and 539.32 eV were assigned to Sb 3d_{3/2} [53,54]. The energy gap value for Sb⁰ and Sb³⁺ were 9.30 and 8.87 eV, respectively, for the Sb₂S₃ electrode, which exhibit slight differences from those for the Ce–Sb₂S₃ electrode. The above results further confirm the effective preparation of the Ce–Sb₂S₃ electrode.

The degradation experiment of PFAAs (PFBA, PFBS, PFOA, and PFOS) was separately conducted under different reaction conditions, and the corresponding results are shown in Fig. S1. The electrochemical degradation of PFBA using Ce/Sb₂S₃ electrode without PMS (only Ce/Sb₂S₃) was stronger than that of Sb₂S₃ electrode (only Sb₂S₃), which was mainly owing to the introduction of Ce increasing catalytic activity (Fig. S1a). From Fig. S1a that a rapid reaction was observed in the Ce/Sb₂S₃ electrode than that in Sb₂S₃ electrode for PFBA degradation within 25 min of electrolysis by adding PMS. In contrast, the PFBA removal rate for electro-Ce/Sb₂S₃/PMS electro-Sb₂S₃/PMS, electro-Ce/Sb₂S₃, and electro-Sb₂S₃ electrodes was 100%, 93.4%, 31.5%, and 26.5%, respectively. It could be observed that only PMS cannot efficiently remove PFAAs within 25 min, and only a 1.92% of PFBA removal rate was achieved. Consequently, the electro-Ce/Sb₂S₃ electrode in the presence of PMS could efficiently and entirely remove PFBA within 25 min, further confirming the great potential of EO with PMS activation. Furthermore, the PFAAs degradation was well-fitted by a pseudo-first-order equation. The apparent rate constant of EO with Ce/Sb₂S₃ electrode with PMS was 0.082 min⁻¹, which was approximately 1.58, 9.11, and 11.7 times that of EO with Sb₂S₃ electrode (0.052 min⁻¹), Ce/Sb₂S₃ electrode (0.009 min⁻¹), and Sb₂S₃ electrode (0.007 min⁻¹), respectively. A similar degradation phenomenon was identified for the degradation of PFBS (Fig. S1b), PFOA (Fig. S1c), and PFOS (Fig. S1d). EO could effectively remove these PFAAs within 25 min, and the Ce/Sb₂S₃ electrode exhibited better performance for the removal of PFAAs than that of Sb₂S₃ electrode. The kinetic rate constant under the EO process for the degradation of PFBA (0.082 min⁻¹) was slightly higher than those of PFBS (0.075 min⁻¹), PFOA (0.069 min⁻¹), and PFOS (0.064 min⁻¹), which was mainly attributed to the relatively low molecular-weight for PFBA brought rapid degradation under EO. The above results suggested a significant synergistic effect when PMS was combined with an electrolysis reaction. As shown in Figs. S2 and 3, the Ce/Sb₂S₃ electrode exhibited much higher oxygen evolution potential (OEP) than that of the Sb₂S₃ electrode in linear sweep voltammetry and cyclic voltammetry curves. A high OEP suggested a high oxidation ability of this electrode [55]. In addition, the DFT calculations (Fig. S4) also confirmed the Ce/Sb₂S₃ electrode with a shorter bond length (Ce-O, 2.109 Å) for electrochemical reaction than that of Sb₂S₃ electrode (Sb-O, 2.322 Å), which indicated quicker electron transfer via the Ce/Sb₂S₃ electrode than Sb₂S₃ electrode during EO process. Consequently, the introduction of Ce into Sb₂S₃ electrode with high OEP could effectively take part in electrochemical reactions for the removal of organics.

The concentration of PMS in the reaction system was directly related to ROS generation [56]. The effect of the PMS concentration (0–5 mM) on PFAAs removal via EO with a Ce/Sb₂S₃ electrode is shown in Fig. S5. The PFBA removal rate was increased from 31.5% to 100% within 25 min by increasing PMS concentration from 0 to 5 mM (Fig. S5a). The corresponding kinetic rate constant was also increased from 0.009 to 0.082 min⁻¹, and the lowest rate constant was achieved at 0 mM, consistent with the results of a previous study [34]. In addition, the effect of PMS concentration on degrading other PFAAs exhibited similar results. The rate constant increased from 0.008 to 0.075 min⁻¹, 0.007–0.069 min⁻¹, and 0.008–0.064 min⁻¹ for the degradation of PFBS (Fig. S5b), PFOA (Fig. S5c), and PFOS (Fig. S5d), respectively. The above findings could be ascribed to the fact that a high concentration of PMS would generating much hydroxyl (\bullet OH) and sulfate (SO₄²⁻) radicals

for PFAAs degradation during electrochemical reaction. However, higher PMS concentrations (e.g., 10 mM) reduced the PFBA kinetic rate constant (0.073 min⁻¹), owing to the quenching reaction between \bullet OH/SO₄²⁻ radicals and excess PMS, as shown in Eqs. 8 and 9 [57]. In addition, similar results were obtained for the degradation of PFBS, PFOA, and PFOS. Thus, PFAAs could be effectively eliminated by EO with a Ce/Sb₂S₃ electrode, and 5.0 mM PMS was the optimal concentration for the electrochemical activation reaction.



The current density was an important parameter in the electrochemical process as it determined the electron transfer efficiency and the amounts of ROS generated during the process. As exhibited in Fig. 2A, almost 100% PFBA removal rate could be achieved at 10 and 20 mA cm⁻² within 25 min electrolysis, and 95.6%, 76.5%, and 31.5% were reached at 5, 2.5, and 0 mA cm⁻², respectively within the same electrolysis time. The PFBA removal rate increased with increasing current density from 0 to 20 mA cm⁻², and the corresponding kinetic rate constants increased from 0.009 to 0.130 min⁻¹. High current density resulted in a high PFBA removal rate because of rapid electron transfer efficiency and ROS generation rate [43]. Meanwhile, the effect of current density on different PFAAs exhibited similar properties. Moreover, high kinetic rate constants of 0.114, 0.121, and 0.108 min⁻¹ could be achieved with a high current density (20 mA cm⁻²) for the degradation of PFBS (Fig. 2B), PFOA (Fig. 2C), and PFOS (Fig. 2D), respectively. The input of high current density would release more electrons, further accelerating the electrochemical reactions and releasing more ROS to degrade PFAAs. The energy consumption condition shown in Fig. 2E could assess and compare the energy utilization efficiency in degrading different organic pollutants at different current densities. The electrical energy per order (EE/O) value drastically decreased with increasing current density, and the value for PFOS was larger than that for the other PFAAs owing to its large molecular weight. The smallest EE/O value (0.36 kWh/m³/order) was achieved by degrading PFBA at a current density of 10 mA cm⁻². In addition, the EE/O values at the current density of 10 mA cm⁻² for the degradation of different PFAAs were slightly higher than those at 20 mA cm⁻². Although the removal efficiency of PFAAs and kinetic rate constants were excellent, a high input current density might consume more energy and leach metal ion from the electrode [58]. Thus, the current density of 10 mA cm⁻² was most suitable for PFAAs degradation, which could also be confirmed by the energy consumption conditions. The effect of input current on the TOC change during EO was also evaluated and exhibited in Fig. 2F. The TOC removal rate enhanced with increasing current density, and PFBA and PFBS exhibited higher TOC removal rate than those of PFOA and PFOS owing to their smaller molecular weight. It should be noted that TOC removal rates at the current density of 10 mA cm⁻² were close to those at 20 mA cm⁻², further confirming that the mineralization efficiencies of PFAAs at 10 and 20 mA cm⁻² were comparable. Consequently, various PFAAs could be effectively removed and mineralized via EO when the current density was 10 mA cm⁻².

3.2. Identification and contribution of reactive species

PFAAs degradation experiments were conducted in the presence of various radical scavengers to identify the primary ROS for PFAAs degradation during EO. Here, MeOH and EtOH were used to scavenge \bullet OH and SO₄²⁻, TBA for \bullet OH, p-benzoquinone for O₂^{•-}, L-histidine and Na₃N for ¹O₂ [59–61]. As illustrated in Fig. 3A, PFBA removal rate rapidly decreased with adding MeOH, and the corresponding kinetic rate constant significantly declined from 0.082 to 0.011 min⁻¹ with increasing MeOH concentration from 0 to 50 mM. In addition, a relatively weak inhibition effect was observed by introducing TBA, as shown in Fig. 3B. The kinetic rate constant was decreased from 0.082 to

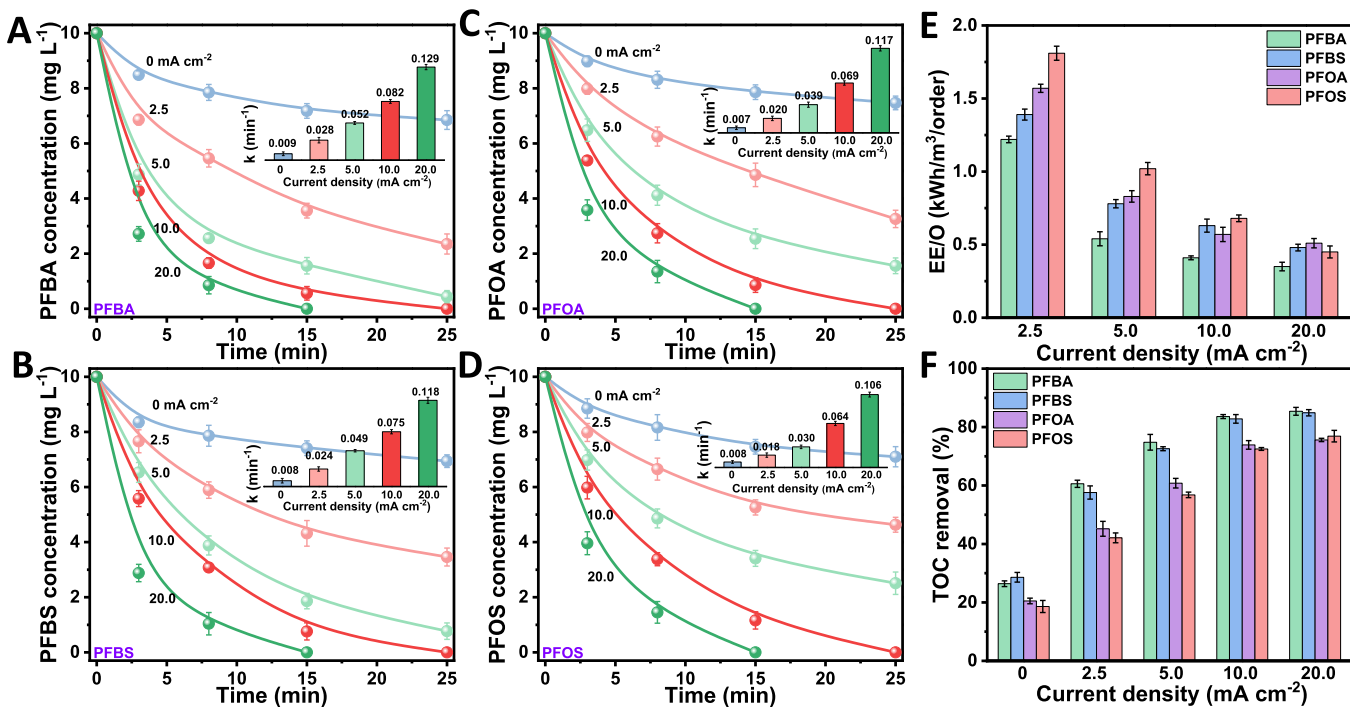


Fig. 2. Effect of different current densities on the degradation of PFAAs: (A) PFBA, (B) PFBS, (C) PFOA, and (D) PFOS. The insets of (A–D) represent the bar graphs of the reaction kinetic rate at different current densities. (E) Energy consumption level and (F) TOC removal rate at different current densities. Conditions: initial PFAAs concentration = 10 mg L⁻¹; initial PMS concentration = 5 mM L⁻¹; temperature = 28 °C.

0.025 min⁻¹ with increasing TBA concentration from 0 to 50 mM. Furthermore, when MeOH concentration was 50 mM, the kinetic rate constants of PFBS, PFOA, and PFOS were reduced to 0.010, 0.007, and 0.008 min⁻¹ (Fig. 3C, E, and G). Similarly, introducing TBA (50 mM) decreased the kinetic rate constants from 0.075 to 0.021 min⁻¹ for PFBS (Fig. 3D), from 0.069 to 0.019 min⁻¹ for PFOA (Fig. 3F), and from 0.064 to 0.019 min⁻¹ for PFOS (Fig. 3H). The above results indicate the involvement of •OH and SO₄^{•-} radicals for PFAAs degradation during EO. The other key ROS was also explored, as shown in Fig. S6. The kinetic rate constant for PFAAs did not exhibit noticeable change by adding LH, BQ, and Na₃N, suggesting O₂^{•-} and ¹O₂ not involved in PFAAs degradation during EO. Adding EtOH also resulted in a significant decline in kinetic rate constants for the degradation of various PFAAs. Consequently, we could confirm the dominant contributions of •OH and SO₄^{•-} for PFAAs degradation. According to the scavenging experiments and the change in the kinetic rate constants, we calculated the contribution of different ROS. The •OH, and SO₄^{•-} radicals were completely quenched in the presence of excessive MeOH, and the DET was responsible for PFBA degradation and the contributions degree of DET was achieved based on the kinetic rate constant [0.011/0.082]. The •OH radical was completely quenched in the presence of excessive TBA, and DET and SO₄^{•-} radical were responsible for PFBA degradation. The corresponding contributions degree of •OH radical was calculated based on the kinetic rate constant [(0.082–0.025)/0.082]. Based on the contribution degree of DET and •OH radical, the contribution degree of SO₄^{•-} radical was also calculated [100%–13.3%–69.5%]. As illustrated in Fig. 3I, the contribution degree of DET, SO₄^{•-}, and •OH radicals for removing PFBA were 13.4%, 17.1%, and 69.5%, respectively. These ROS contributed similarly to PFBA in removing PFBS, PFOA, and PFOS, and •OH radicals showed a greater contribution for removing PFAAs than DET and SO₄^{•-} radicals. Overall, DET, •OH, and SO₄^{•-} radicals were important in degrading PFAAs, and •OH was the dominant ROS for removing PFAAs.

Next, the steady-state concentration of different ROS during electro-activation of PMS were quantified by using NB and ATZ as the probe compounds. As exhibited in Fig. S41, the concentrations of •OH, and

SO₄^{•-} radicals was detected in the electrochemical system with different electrodes. In the Sb₂S₃ electrode system, the concentrations of •OH, and SO₄^{•-} radicals was 0.97×10^{-11} M and 0.34×10^{-11} M, respectively. For the Ce/Sb₂S₃ electrode system, the yield of •OH, and SO₄^{•-} radicals increased to 1.68×10^{-11} M and 0.34×10^{-11} M, respectively. Obviously, the introduction of Ce greatly boosted the generation of ROS and •OH radical showed much higher concentration than that of SO₄^{•-} radical. In addition, the steady-state concentration of ROS was consistent with the contributions of ROS to the degradation of PFAAs. Consequently, the Ce/Sb₂S₃ electrode was effective to the degradation of PFAAs.

To further verify the existence of •OH and SO₄^{•-} radicals during EO, in-situ EPR measurements were conducted using DMPO as the spin-trapping agent. As exhibited in Fig. 4A, no apparent definable peaks were observed when only PMS and DMPO were added to the electrolyte, which was not electrolyzed (0 min), suggesting PMS alone cannot generate reactive radicals [62]. The input current of 10 mA cm⁻² yielded six- (1:1:1:1:1:1) and four-lined (1:2:2:1) peaks, which were assigned to DMPO-SO₄^{•-} (with $a_N = 13.2$ G, $a_H = 9.6$ G, $a_H = 1.48$ G, $a_H = 0.78$ G) [63] and DMPO-•OH spin adduct (with $a_N = a_H = 14.9$ G) [56], respectively, indicating the generation of DMPO-SO₄^{•-} and DMPO-•OH spin adducts during EO for PFBA degradation. In addition, the peak intensity of DMPO-SO₄^{•-} was relatively weaker than that of DMPO-•OH, suggesting more •OH radicals were generated than SO₄^{•-}. The peak intensity for DMPO-•OH slightly increased with the reaction time, indicating the continuous generation of •OH radical during EO. In addition, the EPR spectra of PFBS (Fig. 4B), PFOA (Fig. 4C), and PFOS (Fig. 4D) were detected, and these spectra exhibited similar characteristics to PFBA, further demonstrating the existence and generation of these active radicals during EO. Furthermore, different gases were bubbled into the electrolyte for 30 min to study the origin of the O element in •OH and SO₄^{•-} radicals. As shown in Fig. 4E, the kinetic rate constant of PFBA, PFBS, PFOA, and PFOS remained stable with the addition of Ar, N₂, Air, and O₂. Further, the corresponding TOC removal rate was also evaluated, and no apparent fluctuation was observed in mineralizing these PFAAs by adding different gases (Fig. 4F). The above

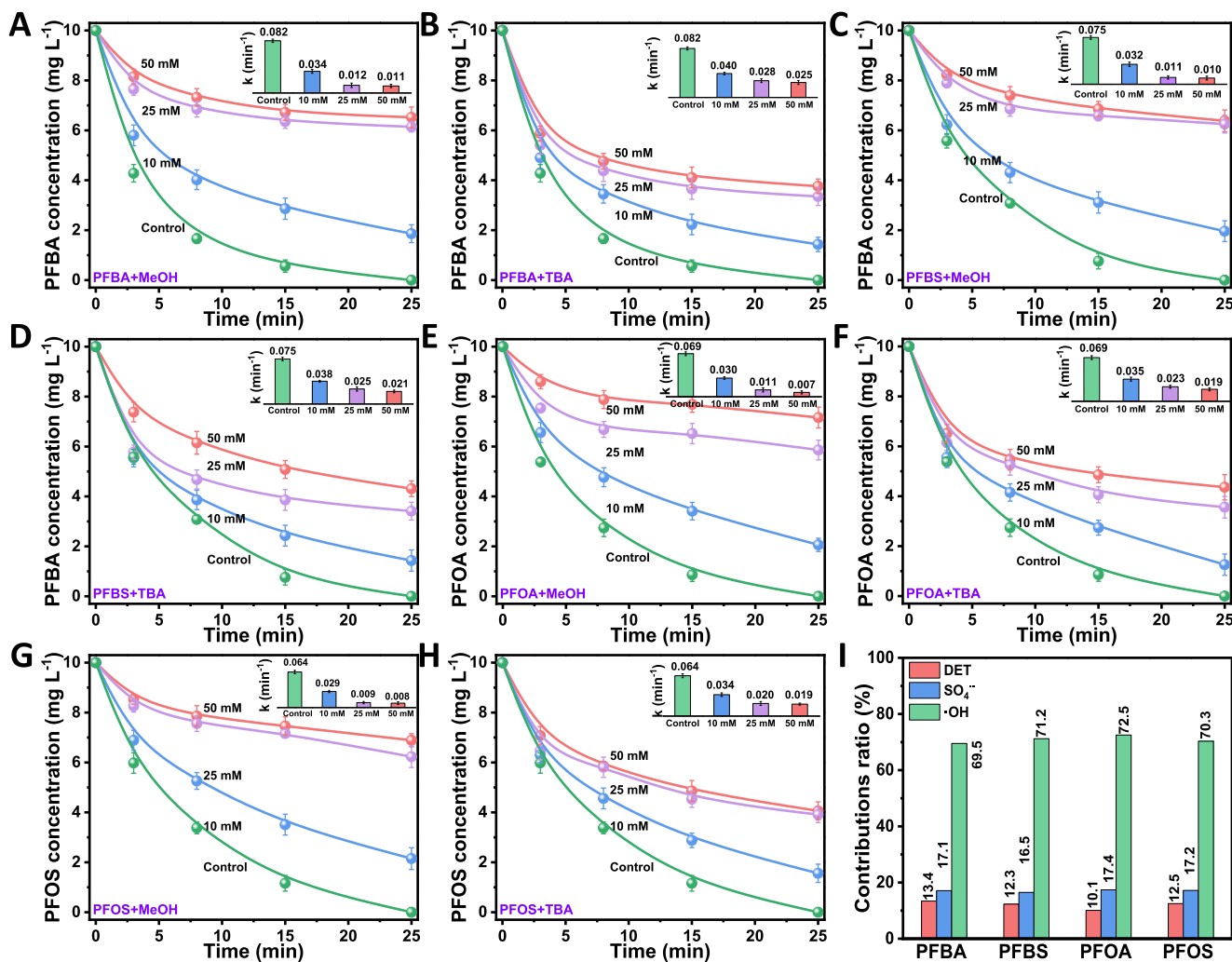


Fig. 3. Effect of different scavengers on PFAAs degradation: (A) PFBA + MeOH, (B) PFBA + TBA, (C) PFBS + MeOH, (D) PFBS + TBA, (E) PFOA + MeOH, (F) PFOA + TBA, (G) PFOS + MeOH, and (H) PFOS + TBA. The insets represent the kinetic rate constant as a function of scavenger concentration. (I) Contribution of different active species on PFAAs degradation. Conditions: initial PFAAs concentration = 10 mg L⁻¹; current density = 10 mA cm⁻²; initial PMS concentration = 5 mM L⁻¹; temperature = 28 °C.

findings revealed that the O element in $\bullet\text{OH}$ and SO_4^{2-} radicals was not from an electrochemical reaction of dissolved oxygen in the electrolyte. Consequently, EO could effectively remove or degrade various PFAAs by the generated active radicals and released electrons.

3.3. Reaction mechanism

DFT calculations were used to further investigate the reaction mechanism and electron transfer pathway during EO. Interestingly, there was a considerable variation in the adsorption energy of PMS onto different sites, as shown in DFT calculations. Fig. 5A–C exhibited the optimal configurations of PMS adsorption on different sites in Ce/Sb₂S₃ electrode, such as the S site (Fig. 5A), Sb site (Fig. 5B), and Ce site (Fig. 5C). On the Sb₂S₃ electrode, the S site (Fig. 5D) and Sb site (Fig. 5E) existed. The adsorption energy for Ce/Sb₂S₃ electrode was lower than those of the Sb₂S₃ electrode, suggesting that PMS preferentially adsorbed on the Ce/Sb₂S₃ electrode. These results also indicated that the structural modification of Sb₂S₃ with Ce enhanced the molecular binding ability of the Ce/Sb₂S₃ electrode during an electrochemical reaction. As exhibited in Fig. 5F, the Ce adsorption site on Ce/Sb₂S₃ electrode for PMS achieved lower adsorption energy (1.530 eV) than those of Sb (1.863 eV) and S sites (2.655 eV), indicating some electrochemical reaction was much easier to be occurred in Ce site than Sb or S sites in Ce/Sb₂S₃.

Sb₂S₃ electrode. Consequently, the Ce site on the Ce/Sb₂S₃ electrode showed the most optimal affinity for adsorbing PMS in the electrochemical reaction.

Furthermore, the free radical generation mechanism during EO was evaluated using DFT calculations, as shown in Fig. 6A. A low free energy of 1.530 eV was achieved when PMS was adsorbed on the Ce site of the Ce/Sb₂S₃ electrode. As exhibited in Fig. S42, the relatively higher free energy of 3.428 eV was obtained when PMS was adsorbed on the Sb₂S₃ electrode. And then, an electron was abstracted from the adsorbed PMS molecule resulting in a formation of $\text{SO}_4^{2-}\text{-Ce/Sb}_2\text{S}_3$ and $\bullet\text{OH}$ radical with a free energy of 0.486 eV. In comparison, the free energy was 1.371 eV for the formation of $\text{SO}_4^{2-}\text{-Sb}_2\text{S}_3$. Subsequently, the $\text{SO}_4^{2-}\text{-Ce/Sb}_2\text{S}_3$ structure would adsorb a water molecule to generate the $\text{HSO}_4^-\text{-Ce/Sb}_2\text{S}_3$ structure and a $\bullet\text{OH}$ radical (0.588 eV). Obviously, the generation of $\bullet\text{OH}$ radical and $\text{HSO}_4^-\text{-Sb}_2\text{S}_3$ structure at the Sb₂S₃ electrode needed the energy of 3.225 eV. Finally, a SO_4^{2-} radical would be released owing to the continuous attack of the transferred electron during EO (5.763 eV). The release of SO_4^{2-} radical at the Sb₂S₃ electrode achieved much higher energy of 7.704 eV than that in the Ce/Sb₂S₃ electrode. However, the high free energy was not beneficial to the generation of active radicals. Low free energy for the Ce/Sb₂S₃ electrode would quickly generate active radicals to attack organic pollutants. Thus, the Ce/Sb₂S₃ electrode exhibited better electrochemical performance than that of the Sb₂S₃

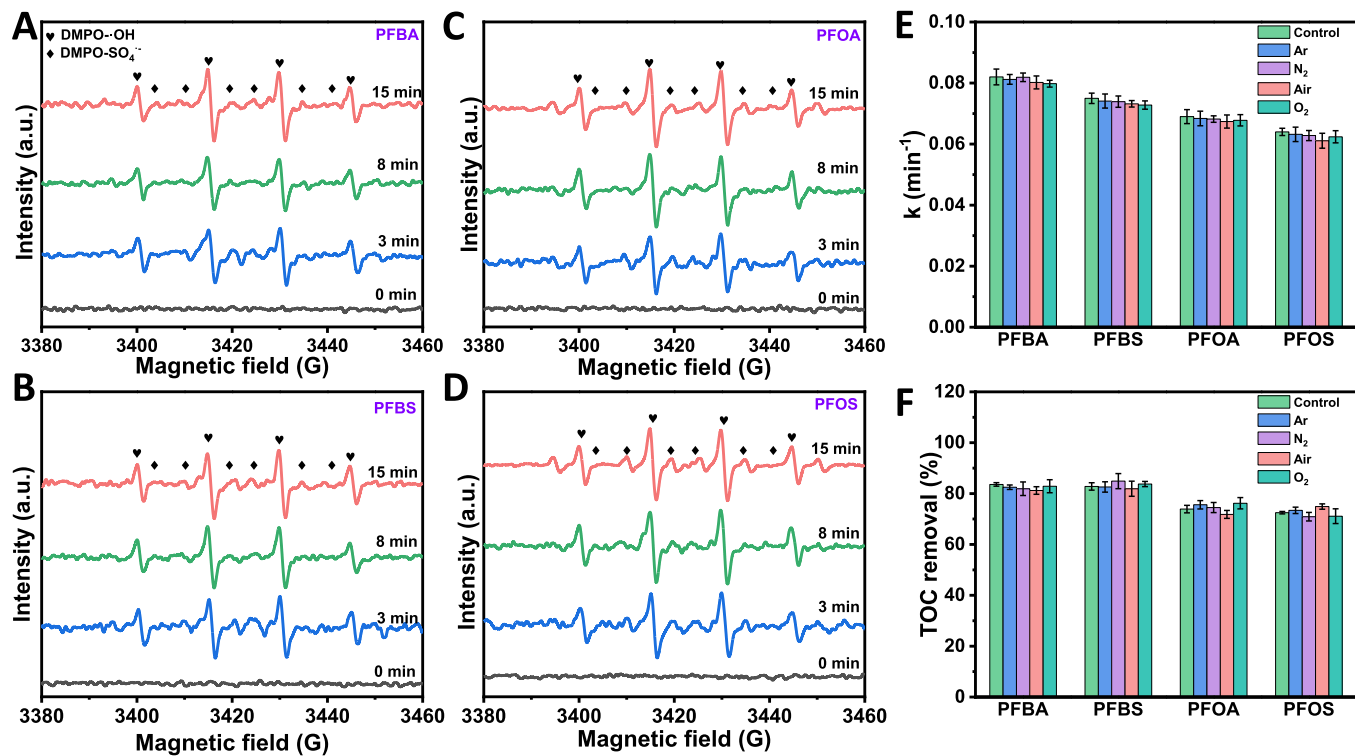


Fig. 4. EPR spectra and reaction performance. EPR spectra of (A) PFBA, (B) PFBS, (C) PFOA, and (D) PFOS; kinetic rate constant and the corresponding TOC removal rate in the presence of various gases. DMPO was used as a trapping agent. Conditions: initial PFAAs concentration = 10 mg L⁻¹; current density = 10 mA cm⁻²; initial PMS concentration = 5 mM L⁻¹; temperature = 28 °C. DMPO was used as a trapping agent for EPR test.

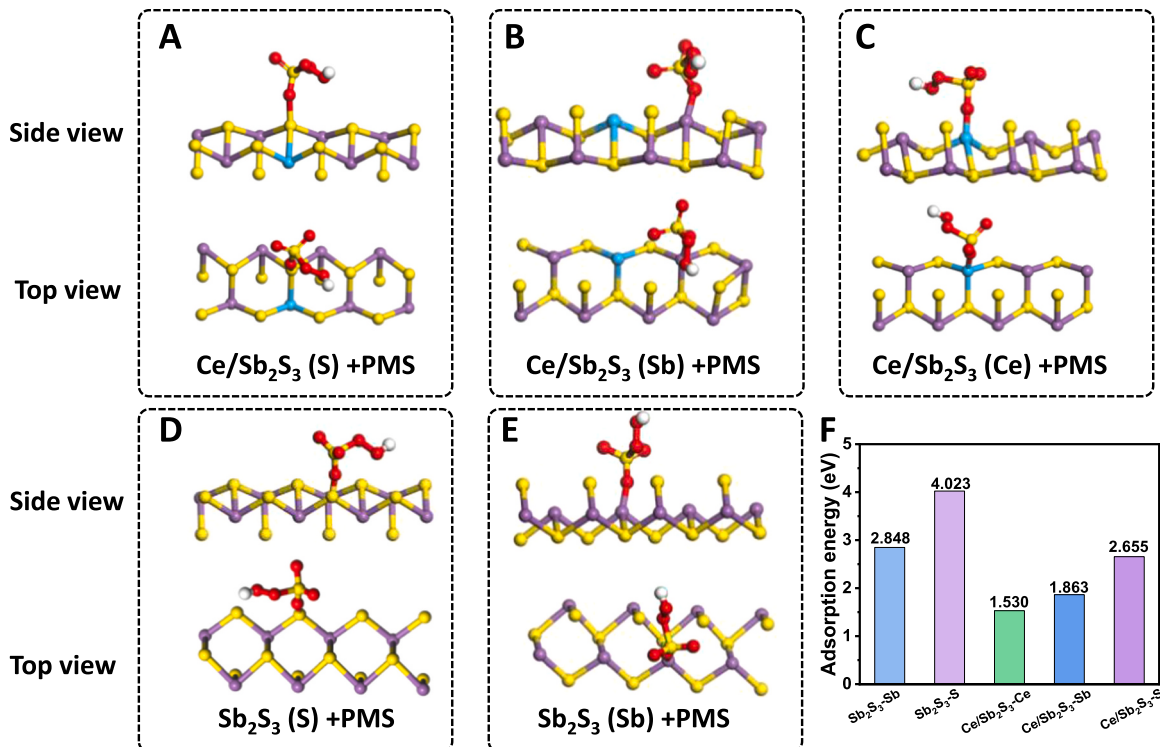


Fig. 5. PMS adsorbed on different active sites on the different electrodes. (A) Ce/Sb₂S₃ (S), (B) Ce/Sb₂S₃ (Sb), (C) Ce/Sb₂S₃ (Ce) (D) Sb₂S₃ (S), and (E) Ce/Sb₂S₃ (Sb). (F) The adsorption energy of PMS on various active sites.

electrode. Here, the electron transfer and attack were identified during the active radical generation, and no metal ions were leached from the electrode surface, further demonstrating the stability of this electrode

during EO. The low free energy further proved thermodynamical feasibility of generating active radicals.

The electron transfer played an important role in producing active

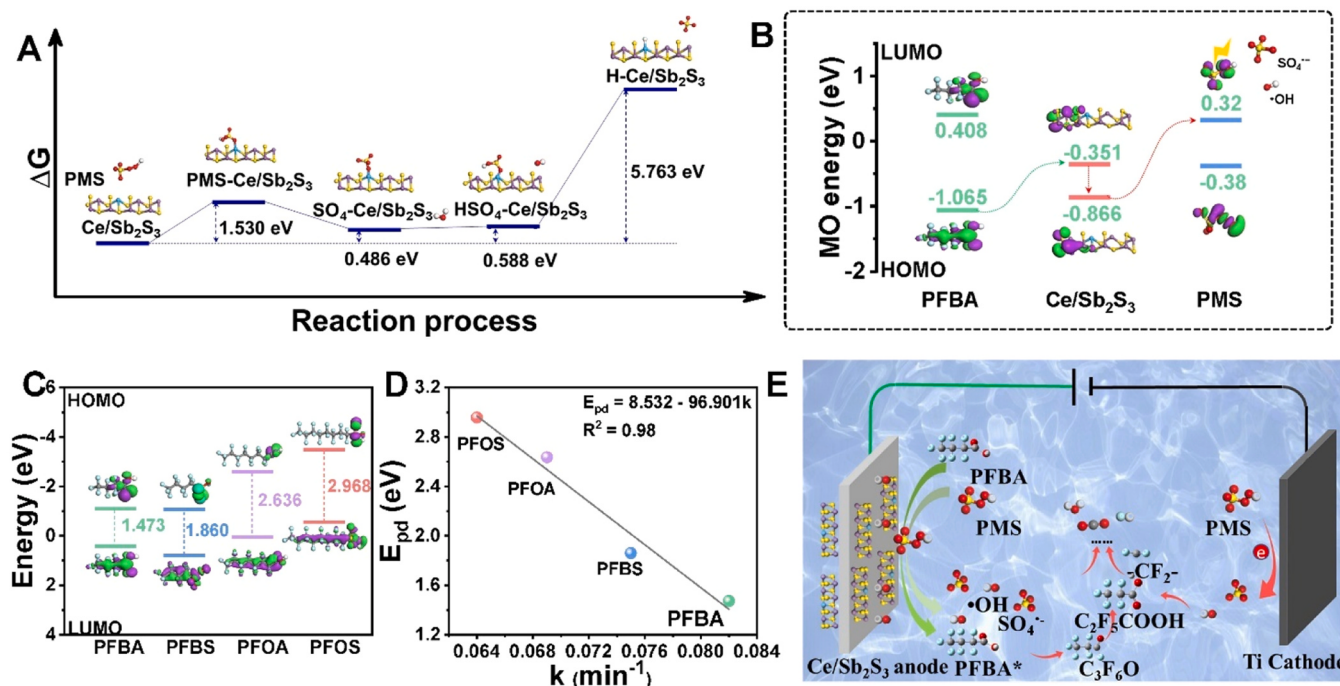


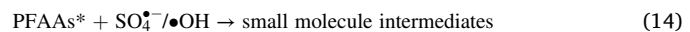
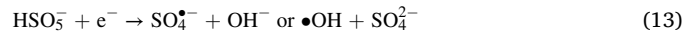
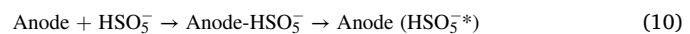
Fig. 6. Radical generation pathway and molecular orbital. (A) Computed free energy profiles for the species assumed to be involved in generating active free radicals. (B) The electron transfer pathway. (C) HOMO and LUMO energy levels of different PFAAs. (D) Correlation between potential differences and kinetic rate constant. (E) The potential degradation mechanism of PFAAs (PFOS as an example) during EO process.

radicals for PFAAs degradation during EO, and the corresponding electron transfer pathway is clarified and exhibited in Fig. 6B. The optimal molecules of PFBA, PMS, Ce/Sb₂S₃, $\bullet\text{OH}$ and $\text{SO}_4^{\bullet-}$, and the corresponding molecular orbital energy between the highest occupied molecular orbital (HOMO) and lowest unoccupied molecular orbital (LUMO) was calculated using DFT. Herein, Ce/Sb₂S₃ had a narrow energy gap between HOMO and LUMO, which beneficial to electron transfer. As illustrated in Fig. 6B, the HOMO of PFBA (-1.065 eV) was more negative than the LUMO of Ce/Sb₂S₃ (-0.351 eV), and the HOMO of Ce/Sb₂S₃ (-0.866 eV) was also more negative than the LUMO of PMS (0.32 eV). These results indicated that the electron transfer from PFBA to PMS via Ce/Sb₂S₃ was energetically favorable.

To explore the relationship between molecular orbitals and degradation kinetic rate constants, the HOMO and LUMO of PFBA, PFBS, PFOA, and PFOS were calculated by DFT calculations. As shown in Fig. 6C, PFOS (2.968 eV) and PFOA (2.636 eV) exhibited larger HOMO-LUMO potential differences than those of PFBA (1.473 eV) and PFBS (1.860 eV), meaning PFOA and PFOS have longer electron transfer distance than those of PFBA and PFBS. The long-distance electron transfer was not beneficial for a rapid electrochemical reaction. This finding can be confirmed by the degradation kinetic rate constant as shown in Fig. S1, in which PFOA (0.069 min^{-1}) and PFOS (0.064 min^{-1}) achieved relatively lower kinetic rate constants than those of PFBA (0.082 min^{-1}) and PFBS (0.075 min^{-1}). The data were fitted between the rate constant of different PFAAs and HOMO-LUMO potential difference and demonstrated a linear relationship with a linear regression coefficient (R^2) of 0.98 (Fig. 6D). The relationship between rate constant and potential difference exhibited a negative correlation, implying the potential difference of HOMO-LUMO in these PFAAs determined their degradation kinetic rate. These results not only elucidated the importance of potential differences in degrading organic pollutants but also provided worthwhile insight into exploring various organic pollutants at the molecular level.

Considering the above investigations, we proposed a potential reaction mechanism for PFAAs degradation during EO (Fig. 6E). Initially, PMS was adsorbed on the surface of the Ce/Sb₂S₃ to form a special

transition state structure (HSO_5^*) because of an electrochemical effect (Eq. 10). Meanwhile, the formed Anode (HSO_5^*) would be decomposed to generate $\bullet\text{OH}$ and $\text{SO}_4^{\bullet-}$ radicals (Eq. 11). In addition, PFAAs would lose an electron to form an unstable PFAAs* radicals due to the strong oxidation ability of anode electrode (Eq. 12), and the generated PFAAs* was very easy to be attacked by active radicals. Meanwhile, the electron would be transferred from the unstable PFAAs* to PMS in solution, and the PMS received electrons could be decomposed into $\bullet\text{OH}$ and $\text{SO}_4^{\bullet-}$ (Eq. 13). The generated active radicals would attack the unstable PFAAs* radicals to form small molecule intermediates. After a series of reactions, the PFAAs would be decomposed from large molecules into small molecules and finally into CO_2 , H_2O , and F^- ions (Eq. 14).



3.4. Degradation pathway of PFAAs

A previous study demonstrated that the substituent groups containing hydroxyl and sulfonic groups in the organic pollutant molecules could affect their degradation by controlling the ESP, mainly owing to the electrons on the molecular surface affecting the electrophilic attack of active radicals [56]. As shown in Fig. 7A-E, the ESP distribution and the corresponding surface area of PFAAs were obtained by DFT calculations. In addition, a significant linear correlation was observed between the PFAAs degradation rate constant and the ESP area based on the Spearman correlation analysis (Fig. 7F). The ESP of PFAAs was mainly governed by the positive potential on the periphery of the molecule, and the negative potential in the substituent groups (-OOH

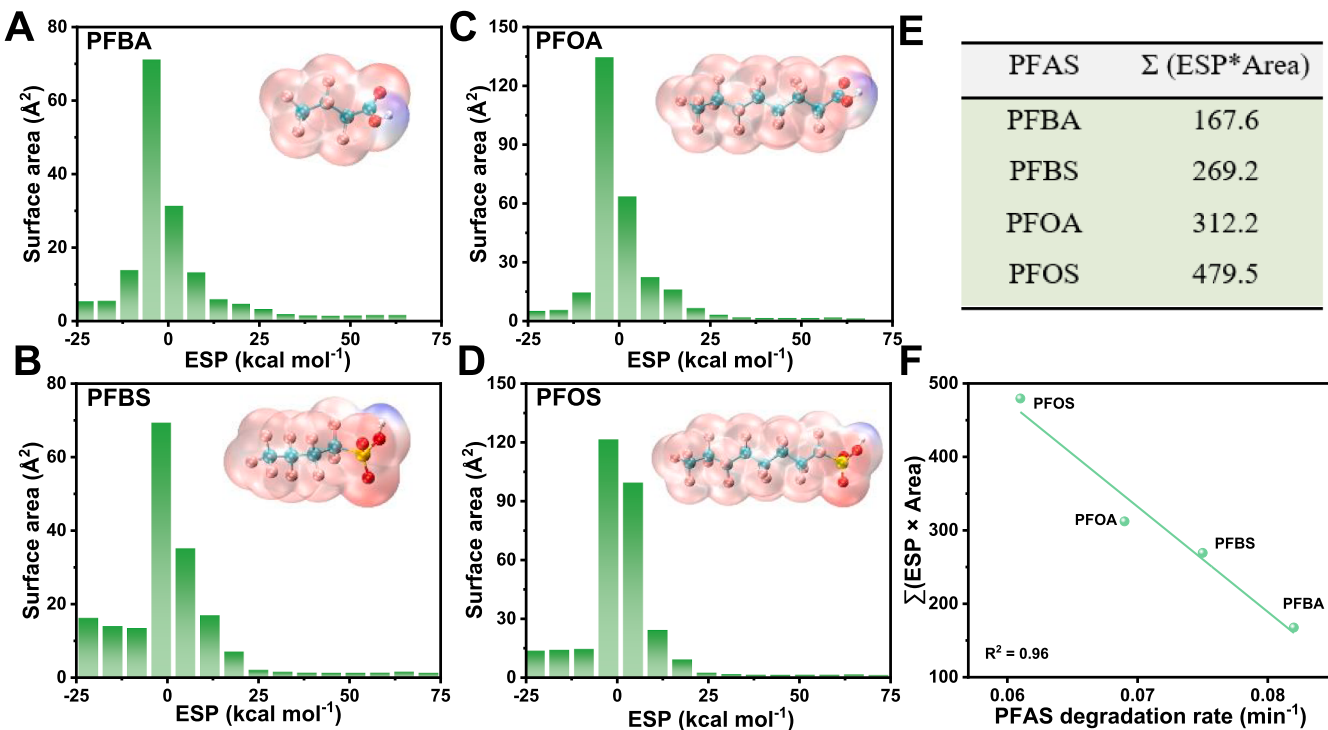


Fig. 7. The electrostatic potential (ESP) distribution of different PFAAs. (A) PFBA, (B) PFBS, (C) PFOA, and (D) PFOS. (E) The extreme point sum of PFAAs in ESP and its corresponding area. (F) The linear fit between the PFAAs degradation rate and ($\Sigma (\text{ESP} \times \text{Area})$.

and $-\text{SO}_3\text{H}$ in PFAAs. These substituents would be sufficiently conducive to attacking $\bullet\text{OH}$ and SO_4^{2-} radicals. However, the presence of positive potential on the periphery of the molecule was a great obstacle to attract these free radicals. These groups of $-\text{OOH}$ and $-\text{SO}_3\text{H}$ on PFAAs would bring high ESP values (positive potential) of PFBA (167.6), PFBS (269.2), PFOA (312.2), and PFOS (479.5), which was not beneficial for electrophilic $\bullet\text{OH}$ and SO_4^{2-} radicals receiving electrons, further resulting in poor removal rate. Herein, the addition of current would break the stable structure to form unstable PFAAs*, as explained in the reaction mechanism.

DFT calculations provided deep insights into PFAAs degradation during EO, where a series of oxidations related to electrophilic and nucleophilic reactions took place involving electron transfer, $\bullet\text{OH}$, and SO_4^{2-} radicals. The optimal molecular structure and Fukui index (f^-) representing the charge distribution of PFAAs are shown in Fig. S7 and table S1–4. For PFBA (Fig. S7a), a higher f^- value was achieved for the 11 C atom than that for the other C atoms, suggesting that 11 C was the most susceptible site to be attacked by the electrophilic species ($\bullet\text{OH}$ and SO_4^{2-} radicals). Furthermore, we can observe f^- values for 11 C (0.0906) from PFBS (Figs. S7b), 8 C (0.0535) from PFOA (Fig. S7c), and 23 C (0.0246) from PFOS (Fig. S7d), which were larger than the other carbons in carbon-chains. Hence, these C atoms in the C-chains were the key attacking point. In addition, the 13 O atom in PFBA, 13 O in PFBS, 10 O in PFOA, and 27 O in PFOS achieved the maximum f^- value, indicating these sites were easily attacked. The above results could also be proved by the ESP distribution of different PFAAs (Fig. 7), where the regions surrounded by oxygen-containing groups preferred to attract $\bullet\text{OH}$ and SO_4^{2-} . Based on these results and LC-MS, the possible degradation pathway of PFAAs was proposed, as shown in Fig. 8.

For PFBA degradation (Fig. 8A), PFBA firstly would be transformed into PFBA* due to the attack of the electron under the electrochemical effect (Eq. 15). Subsequently, the formed PFBA* would be attacked by $\bullet\text{OH}$ radical to form $\text{C}_3\text{F}_7\text{O}$ (Eq. 16). DFT calculations explored an activation barrier of 3.23 kcal mol⁻¹ for DET from PFBA* to $\text{C}_3\text{F}_7\text{O}$, as exhibited in Fig. 8F. The above results confirmed that once PFBA* was formed via DET, the radical would attack the 11 C site to form $\text{C}_3\text{F}_7\text{O}$.

The $\text{C}_3\text{F}_7\text{O}$ would undergo hydrolysis to generate $\text{C}_2\text{F}_5\text{COOH}$ and release another F ion (Eq. 17) with an activation barrier of 6.98 kcal mol⁻¹ and total energy barrier of 17.24 kcal mol⁻¹. Finally, the formed $\text{C}_2\text{F}_5\text{COOH}$ can be mineralized to CO_2 and HF by repeating the COF-unzipping cycle under electrochemical transfer, decarboxylation reaction, radical attack, and hydrolysis (Eq. 18).

For PFBS degradation (Fig. 8B), the PFBS molecule was easy to lose an electron leading to the formation of $\text{C}_4\text{F}_9\text{SO}_3^*$ due to the strong oxidation effect of the anode (Eq. 19). The loss of an electron in the PFBS structure brought a stretching of the C-S bond, but the C-S bond in $\text{C}_4\text{F}_9\text{SO}_3^*$ structure exhibited much lower bond energy than those of C-C and C-F bond [64]. Thus, the C-S bond in $\text{C}_4\text{F}_9\text{SO}_3^*$ was further attacked, and $\text{C}_4\text{F}_9\text{SO}_3^*$ was decomposed to $\text{C}_4\text{F}_9\text{O}$ (Eq. 20) via the attack of $\bullet\text{OH}$ radical with an activation energy of 6.21 kcal mol⁻¹ (Fig. 8G) [65]. After an important hydrolysis reaction and hydrolysis, $\text{C}_4\text{F}_9\text{O}$ would be transformed to $\text{C}_3\text{F}_7\text{COOH}$ (Eq. 21). The activation energy and total energy barrier of these process were 5.28 and 13.57 kcal mol⁻¹, respectively (Fig. 7G). With the continuous removal of –COF unit, PFBS was mineralized into CO_2 and F ion (Eq. 22).

The degradation of PFOA (Fig. 8C) and PFOS (Fig. 8D) exhibited similar chemical structures and properties, and the corresponding degradations processes were also similar. PFOA and PFOS would undergo multiple cycles (text S1) with the continuous decomposition of –COF units due to large molecular structures and long carbon chains. In addition, the calculated activation energies and total free energy for the degradation of PFOA (Fig. S8A) and PFOS (Fig. S8B) demonstrated the reliability of the degradation reaction. According to the above results, the degradation processes of different PFAAs were generalized. As shown in Fig. 8E, the PFAAs ($\text{C}_n\text{F}_{2n+1}\text{COOH}/\text{C}_{n+1}\text{F}_{2n+3}\text{SO}_3\text{H}$, $n = 3$ or 7) molecules were easy to lose the electron to form $\text{C}_n\text{F}_{2n+1}\text{COO}^*/\text{C}_{n+1}\text{F}_{2n+3}\text{SO}_3^*$ due to the strong oxidation effect of the anode, and then the formed C-C bond adjacent to the O atom in $\text{C}_n\text{F}_{2n+1}\text{COO}^*$ and the C-S bond in $\text{C}_{n+1}\text{F}_{2n+3}\text{SO}_3^*$ was further attacked to form $\text{C}_n\text{F}_{2n}\text{O}$ via radical attack reaction. The $\text{C}_n\text{F}_{2n}\text{O}$ would generate $\text{C}_{n-1}\text{F}_{2n-1}\text{COOH}$ and lose F ion via hydrolysis. Finally, the $\text{C}_{n-1}\text{F}_{2n-1}\text{COOH}$ would be completed mineralize to CO_2 and F ion. Overall, various PFAAs containing PFBA,

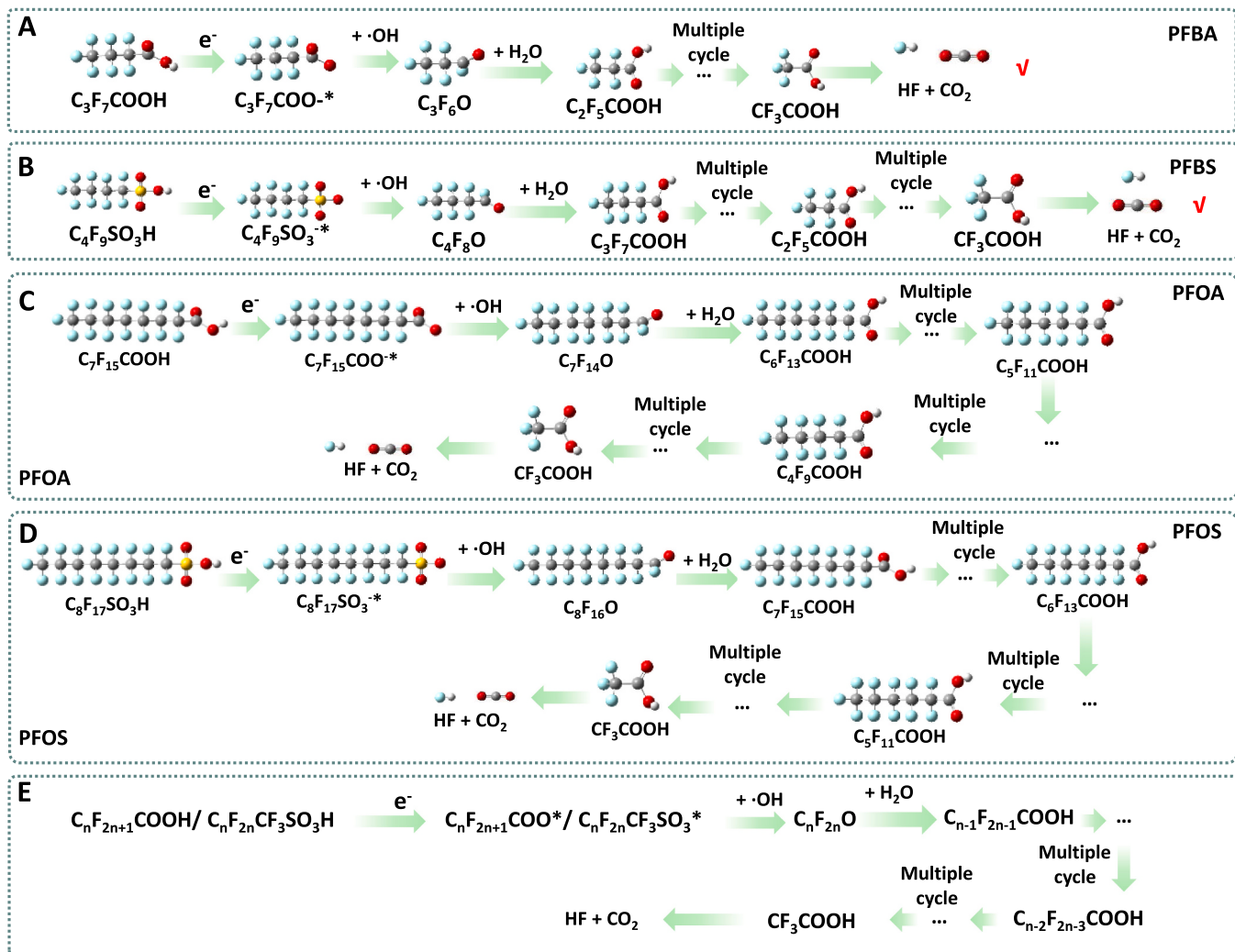
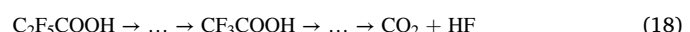
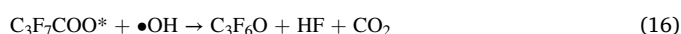


Fig. 8. Degradation pathway of PFAAs. The potential degradation pathways of (A) PFBA, (B) PFBS, (C) PFOA, and (D) PFOS. (E) The generalizing degradation process ($n = 3$ or 7). The free energy profiles of the proposed intermediates and TSs for (F) PFBA and (G) PFBS degradation during EO process.

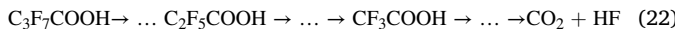
PFBS, PFOA, and PFOS could be completely mineralized into small molecules, even CO_2 and F^- ion by repeating the COF-unzipping cycle via electron transfer, decarboxylation/desulfurization, radical attack reaction, and hydrolysis reaction.

For PFBA:



For PFBS:





3.5. Stability and applied potential

The explorations above confirmed that the degradation of PFAAs could release fluorine ions, and the fluorine mass balance could further clarify the degradation effectiveness. As presented in Fig. 9A, the fluorine mass balance calculated from $m_{\text{F-degraded PFAAs}} + m_{\text{F-intermediates}} + m_{\text{F ion}}/m_{\text{F-initial PFAAs}}$ were in the 100%–89.8% during EO within 25 min. The PFBA could be quickly removed with reaction time, and the concentration of the fluorine ions continuously increased at a prolonged rate in the presence of PMS (from 0% to 83.5%), suggesting PMS was an important activator in precipitate with electrochemical reaction and the presence of PMS could greatly enhance PFBA degradation. In addition, a minor decrease in fluorine mass balance was observed because the generated intermediates from degradation had not been determined or

quantified. In addition, the fluorine mass balance for the degradation of PFBS (Fig. 9B), PFOA (Fig. 9C), and PFOS (Fig. 9D) was in the range of 100%–87.7%, 100%–84.8%, and 100%–82.9%, respectively. The corresponding fluorine ion concentration was increased from 0% to 81.7%, 77.7%, and 73.6% for PFBS, PFOA, and PFOS, respectively. A similar change for fluorine ions suggested the effectiveness of the electrode for PFAAs degradation during EO. Here, the PFBA degradation was exhibited as an example. As shown in Fig. S9a, the PFBA, TOC, and F ion concentrations in solution were 0, 0.03 mg L⁻¹, and 0.582 mg F L⁻¹, respectively, after 25 min reaction via EO process, suggesting the EO process with Ce/Sb₂S₃ electrode can effectively degrade PFBA to CO₂ and F ions. In addition, the organic intermediates generated during EO were detected by LC-MS/MS. As exhibited in Fig. S9b, the concentration of C₄F₉, C₄F₉OH, C₃F₇OH, C₂F₅OH, and CF₃OH rapidly increased with the reaction time and then significantly declined after 25 min reaction. The results were mainly owing to that the generated PFAAs intermediates were further decomposed to small molecule intermediates, followed by mineralization to CO₂ and F ions, which can be explained by the high TOC removal efficiency of 87.9% at 25 min (Fig. S9b). The F and C mass balance of PFBA was also explored in our work. As shown in

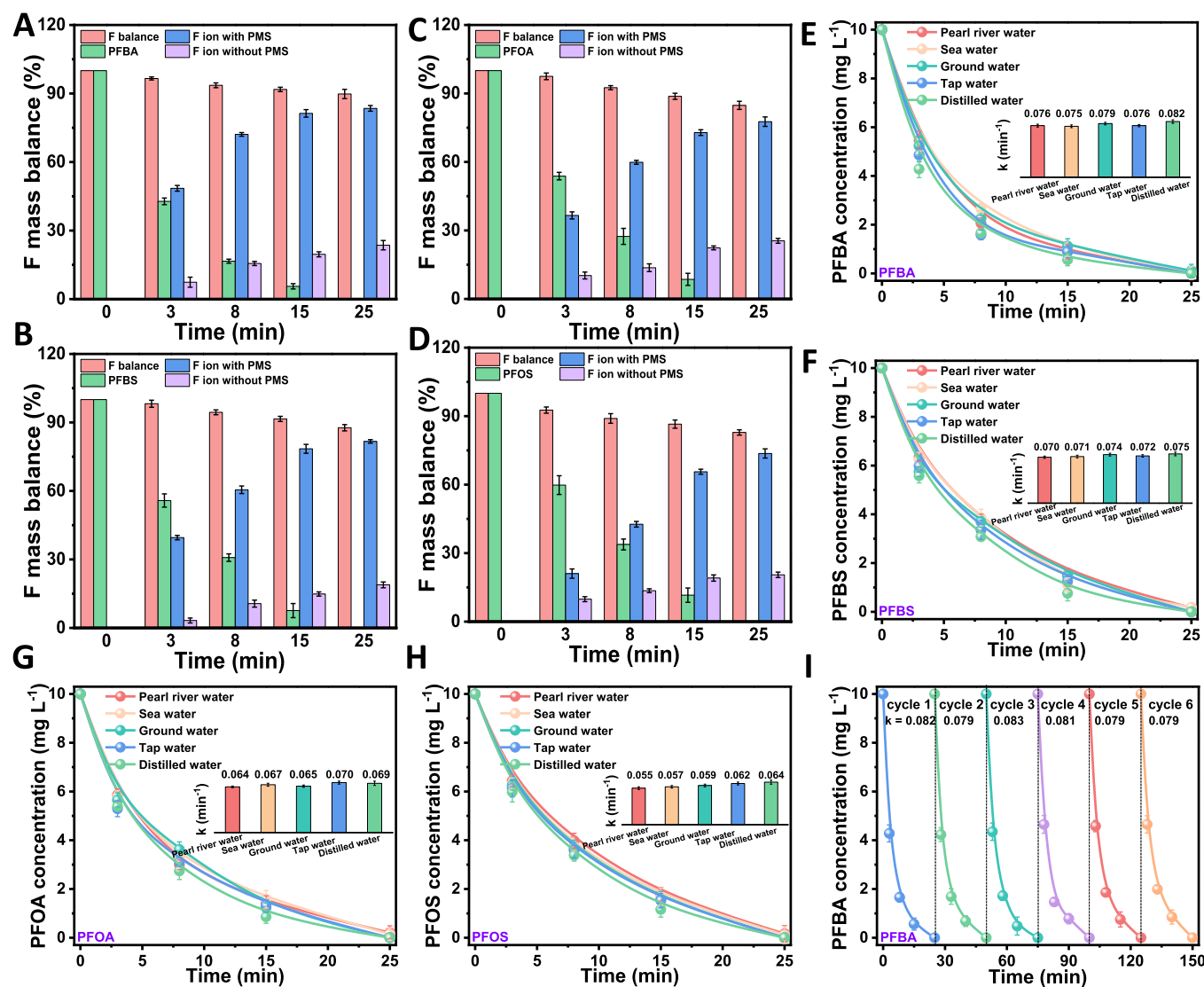


Fig. 9. Mass balance of fluorine and system stability. Mass balance of elemental fluorine with time during EO: (A) PFBA, (B) PFBS, (C) PFOA, and (D) PFOS; Effects of different water environments on the degradation of PFAAs: (E) PFBA, (F) PFBS, (G) PFOA, and (H) PFOS; (I) The reusability and stability of the reaction system on the degradation of PFBA. Conditions: initial PFAAs concentration = 10 mg L⁻¹; current density = 10 mA cm⁻²; initial PMS concentration = 5 mM L⁻¹; temperature = 28 °C.

Fig. S9c, the F mass balance calculated from $m_{F\text{-undegraded PFBA}} + m_{F\text{-intermediates}} + m_{F\text{ ion}})/m_{F\text{-initial PFBA}}$ was in the 100%–89.8% during EO within 25 min. The defluorination ratio was 97.1% after 25 min electrolysis. Likewise, the C mass balance was achieved from $m_{C\text{-undegraded PFBA}} + m_{C\text{-PFBA intermediates}} + m_{TOC\text{-removal}})/m_{C\text{-initial PFBA}}$. The C recovery rate was 100%–90.7% during 25 min electrolysis of PFBA degradation via EO process (**Fig. S9d**), indicating some critical degradation intermediates were detected. Consequently, the high F and C recovery and mass balance further confirmed the mineralization and decomposition of PFAAs in solution via EO process with Ce/Sb₂S₃ electrode.

To further study the application of EO for the degradation and elimination of organic pollutants, EO was conducted with PFAAs in different water matrices containing distilled water, tap water, groundwater, seawater, and pearl-river water. Although there were a variety of background substances in these water matrices, nearly 100% of PFBA degradation could be achieved (**Fig. 9E**). The degradation rate constant of PFBA for seawater (0.075 min^{-1}) and pearl river water (0.076 min^{-1}) was slightly decreased than those of distilled water (0.082 min^{-1}), which was mainly ascribed to the presence of various anions or cations in seawater or pearl water. Similar results could also be observed for the degradation of PFBS (**Fig. 9F**), PFOA (**Fig. 9G**), and PFOS (**Fig. 9H**). Although the rate constant exhibited little decrease, removal efficiencies of these PFAAs were still high. Consequently, EO possessed great potential for PFAAs degradation in actual application.

To assess the stability and reusability of the electrode, multiple cycled experiments were carried out for removing various PFAAs. As exhibited in **Fig. 9I**, the removal efficiency of PFBA showed no significant decrease after six cycles. However, the degradation rate constant was decreased from 0.082 to 0.079 min^{-1} , because the active sites on the surface of the Ce/Sb₂S₃ electrode were occupied by partially degraded intermediates. Furthermore, the removal efficiencies and the corresponding kinetic rate constants of PFBS (**Fig. S10a**), PFOA (**Fig. S10b**), and PFOS (**Fig. S10c**) changed a little after six cycles, confirming excellent stability and recyclability of the Ce/Sb₂S₃ electrode for the elimination of PFAAs.

The surface properties were characterized by XRD and XPS after six cycles to investigate the metal ion leaching from the electrode. As shown in **Fig. S11a**, many diffraction peaks of Ce/Sb₂S₃ assigned to the JCPDS card (PDF#42-1393) [53] had no noticeable change, and the elemental position on the survey spectrum of XPS was also stable before and after use (**Fig. S11b**). Similarly, the peak position of Sb 3d (**Fig. S11c**), Ce 3d (**Fig. S11d**), and S 2p (**Fig. S12**) exhibited a slight shift, and the binding energy difference of these elements was minorly increased from 8.78 to 8.89 eV for Sb³⁺, from 9.27 to 9.29 eV for Sb⁰, from 19.42 to 19.35 eV for Ce⁴⁺, and from 19.88 to 19.69 eV for Ce³⁺. After six-cycles, the concentration of released metal was measured to ~10 ppb in the treated solution by the Inductively Coupled Plasma Mass Spectrometry (ICP-MS), which is much lower than the emission limitation. The above results suggested that the Ce/Sb₂S₃ electrode kept its stable structure and properties, further confirming its great potential for PFAAs degradation during EO.

The removal performance of PFAAs in our studies via EO was compared with some previously reported studies. As exhibited in **Table S5**, the PFAAs removal efficiency and kinetic rate constant of PFAAs degradation in this study was significantly higher than those of 3D graphene-lead oxide electrode [43], nano-ZnO electrode [66], Ti/S-nO₂-Sb electrode [34], macro-porous TiO₂ electrode [33], boron/nitrogen diamond electrode [67], and Ti/SnO₂-Sb₂O₅/PbO₂-PTFE electrode [68]. Although some photocatalyst methods could effectively remove PFAAs, this method would take a long reaction time and achieve a low kinetic rate constant [69–71]. In addition, the removal efficiencies and mineralization degree of PFAAs in our study were much higher than those of BDD, 3D-BDD, and Si/BDD electrodes, [72–75] except for the BDD from Wang et al. report [76]. Although Wang et al. study used a BDD anode FeMnC cathode for oxygen reduction reaction could further enhance the removal of PFOA, this process exhibited a low kinetic rate

constant. Consequently, EO with Ce/Sb₂S₃ electrode was a high-effective and excellent method for removing PFAAs, and it could be used as a potential technology for wastewater treatment and environmental remediation.

4. Conclusions

In summary, the electrochemical oxidation process with PMS activation reaction could efficiently degrade PFBA, PFBS, PFOA, and PFOS within 25 min and achieved high kinetic rate constant of 0.082, 0.075, 0.069, and 0.064 min^{-1} , respectively. Adding PMS and solution temperature significantly enhanced PFAAs degradation, harvesting a high TOC removal rate. The overall analysis from various scavengers' experiments and EPR tests suggested that DET, •OH, and SO₄^{•-} radicals were responsible for the degradation of PFAAs and •OH contributed to over 70% of the PFAAs removal. The Ce/Sb₂S₃ exhibited stronger adsorption ability with PMS and easily transferred electrons from LUMO to HOMO. The electrons were driven by a potential difference between the HOMO of PFBS to the LUMO of PMS via Ce/Sb₂S₃ transfer, and the transferred electrons further decomposed PMS to generate •OH and SO₄^{•-} radicals for effective PFAAs degradation. The quantum chemical calculations indicated the 13 O atom in PFBA, 13 O in PFBS, 10 O in PFOA, and 27 O in PFOS achieved the maximum f value, implying that these sites were vulnerable to be attacked. These PFAAs show similar degradation properties, and they could be degraded by multiple-cycles in the decomposition of -COF and -CO₂/-SO₃H units under the effects of electron transfer, •OH, and SO₄^{•-} radicals. Besides, the TOC removal rate and the fluorine balance confirmed the effective mineralization and defluorination performance of PFAAs via EO. After continuous multiple-cycles for PFAAs degradation, the kinetic rate constant maintained at a stable level and the leaching Ce and Sb ions from the electrode was greatly lower than the emission standard. Overall, EO is a promising technology for the removal and degradation of various PFAAs, with potential applicability in wastewater mineralization and environmental cleansing.

CRediT authorship contribution statement

Hongguo Zhang: Investigation. **Meng Li:** Writing – review & editing, Writing – original draft, Supervision, Investigation, Formal analysis, Data curation. **Shaoqi Zhou:** Project administration. **Wei Han:** Data curation, Conceptualization. **jiayu Song:** Data curation. **Jiliang Cheng:** Resources. **Ce-Hui Mo:** Visualization, Validation, Project administration. **King Lun Yeung:** Visualization, Software, Methodology, Investigation. **Qiong Wu:** Resources. **Zhaoxin Zhang:** Validation.

Declaration of Competing Interest

The authors declare that they have no known competing financial interests or personal relationships that could have appeared to influence the work reported in this paper.

Data Availability

Data will be made available on request.

Acknowledgements

We gratefully thank the financial support from Project Funded by National Natural Science Foundation of China (42007358), National Natural Science Foundation of China of Key Program (42030713), Basic and Applied Basic Research Foundation of Guangdong Province (2020A1515110518), the Hong Kong Scholarship Program (XJ2020059), and China Postdoctoral Science Foundation (2019M663382). KLY acknowledges the Project of Hetao Shenzhen-Hong Kong Science and Technology Innovation Cooperation Zone

(HZQB-KCZYB-20200083). SQZ thanks the project of the State Key Research & Development Project of China (2022YFC3705003) and the Project funded by the Department of Science & Technology of Guizhou Province (2023-115). The authors would like to thank Shyanjia Lab (www.shyanjia.com) for Quantum chemical calculations.

Author contributions

M.L. and J.C. designed and operated the study, M.L. and J.S. wrote and revised the manuscript, H.Z., J.C., Q.W., and Z.Z. helped analyze the experimental conditions, W.H. and S.Z. helped with the analysis of mechanism, K.Y. and C.M. provided valuable suggestions to this study.

Appendix A. Supporting information

Supplementary data associated with this article can be found in the online version at [doi:10.1016/j.apcatb.2024.123983](https://doi.org/10.1016/j.apcatb.2024.123983).

References

- [1] X. Tan, Z. Jiang, W. Ding, M. Zhang, Y. Huang, Multiple interactions steered high affinity toward PFAS on ultrathin layered rare-earth hydroxide nanosheets: Remediation performance and molecular-level insights, *Water Res* 230 (2022) 119558.
- [2] T. Buckley, K. Karanam, H. Han, H.N.P. Vo, P. Shukla, M. Firouzi, V. Rudolph, Effect of different co-foaming agents on PFAS removal from the environment by foam fractionation, *Water Res* 230 (2022) 119532.
- [3] Y. Fang, P. Meng, C. Schaefer, D.R.U. Knappe, Removal and destruction of perfluoroalkyl ether carboxylic acids (PFECA) in an anion exchange resin and electrochemical oxidation treatment train, *Water Res* 230 (2022) 119522.
- [4] L. Wang, J. Lu, L. Li, Y. Wang, Q. Huang, Effects of chloride on electrochemical degradation of perfluorooctanesulfonate by Magnéti phase Ti_4O_7 and boron doped diamond anodes, *Water Res* 170 (2020) 115254.
- [5] X. Tan, G. Chen, D. Xing, W. Ding, H. Liu, T. Li, Y. Huang, Indium-modified Ga_2O_3 hierarchical nanosheets as efficient photocatalysts for the degradation of perfluorooctanoic acid, *Environ. Sci. Nano* 7 (2020) 2229–2239.
- [6] Z. Li, Z.M. Luo, Y. Huang, J.W. Wang, G. Ouyang, Recent trends in degradation strategies of PFOA/PFOS substitutes, *Chemosphere* 315 (2022) 137653.
- [7] J.L. Wilkinson, A.B.A. Boxall, D.W. Kolpin, K.M.Y. Leung, R.W.S. Lai, C. Galban-Malagon, A.D. Adell, Pharmaceutical pollution of the world's rivers, *Proc. Natl. Acad. Sci.* 119 (2022) 2113947119.
- [8] M. Trojanowicz, I. Bartosiewicz, A. Bojanowska-Czajka, T. Szreder, K. Bobrowski, G. Nalecz-Jawecki, S. Me czynska-Wielgosz, H. Nichipor, Application of ionizing radiation in decomposition of perfluorooctane sulfonate (PFOS) in aqueous solutions, *Chem. Eng. J.* 379 (2020) 122303–122320.
- [9] D. Ma, Y. Lu, Y. Liang, T. Ruan, J. Li, C. Zhao, Y. Wang, G. Jiang, A critical review on transplacental transfer of per- and polyfluoroalkyl substances: prenatal exposure levels, characteristics, and mechanisms, *Environ. Sci. Technol.* 56 (2022) 6014–6026.
- [10] H. Tang, W. Zhang, Y. Meng, S. Xia, A direct Z-scheme heterojunction with boosted transportation of photogenerated charge carriers for highly efficient photodegradation of PFOA: Reaction kinetics and mechanism, *Appl. Catal. B Environ.* 285 (2021) 119851.
- [11] E.M. Sunderland, X.C. Hu, C. Dassuncao, A.K. Tokranov, C.C. Wagner, J.G. Allen, A review of the pathways of human exposure to poly- and perfluoroalkyl substances (PFASs) and present understanding of health effects, *J. Expo. Sci. Environ. Epidemiol.* 29 (2019) 131–147.
- [12] J.M. Jian, C. Zhang, F. Wang, X. Lu, F. Wang, E.Y. Zeng, Effect of solution chemistry and aggregation on adsorption of perfluorooctanesulphonate (PFOS) to nano-sized alumina, *Environ. Pollut.* 251 (2019) 425–433.
- [13] P.J. Choi, L. J.Y., P.K. Sing, S.J. Im, A. Jang, A.K. An, Low-pressure volume retarded osmosis for removal of per- and polyfluoroalkyl substances, *Water Res* 194 (2021) 116929.
- [14] M. Li, C.H. Mo, X. Luo, K.Y. He, J.F. Yan, Q. Wu, P.F. Yu, W. Han, N.X. Feng, K. L. Yeung, S.Q. Zhou, Exploring key reaction sites and deep degradation mechanism of perfluorooctane sulfonate via peroxymonosulfate activation under electrocoagulation process, *Water Res* 207 (2021) 117849.
- [15] V.L. Gole, A. Fishgold, R. Sierra-Alvarez, P. Deymier, M. Keswani, Treatment of perfluorooctane sulfonic acid (PFOS) using a large-scale sonochemical reactor, *Separ. Purif. Technol.* 194 (2018) 104–110.
- [16] T.H. Kim, S. Yu, Y. Choi, T.Y. Jeong, S.D. Kim, Profiling the decomposition products of perfluorooctane sulfonate (PFOS) irradiated using an electron beam, *Sci. Total Environ.* 631–632 (2018) 1295–1303.
- [17] N. Merino, Y. Qu, R.A. Deeb, E.L. Hawley, M.R. Hoffmann, S. Mahendra, Degradation and removal methods for perfluoroalkyl and polyfluoroalkyl substances in water, *Environ. Eng. Sci.* 33 (2016) 615–649.
- [18] Z. Sun, C. Zhang, J. Jiang, J. Wen, Q. Zhou, M.R. Hoffmann, UV/ $Fe^{II}NTA$ as a novel photoreductive system for the degradation of perfluorooctane sulfonate (PFOS) via a photoinduced intramolecular electron transfer mechanism, *Chem. Eng. J.* 427 (2022) 130923.
- [19] H. Zhang, P. Li, A. Zhang, Z. Sun, J. Liu, P. Heroux, Y. Liu, Enhancing interface reactions by introducing microbubbles into a plasma treatment process for efficient decomposition of PFOA, *Environ. Sci. Technol.* 55 (2021) 16067–16077.
- [20] L. Yang, L. He, J. Xue, Y. Ma, Z. Xie, L. Wu, M. Huang, Z. Zhang, Persulfate-based degradation of perfluorooctanoic acid (PFOA) and perfluorooctane sulfonate (PFOS) in aqueous solution: Review on influences, mechanisms and prospective, *J. Hazard. Mater.* 393 (2020) 122405.
- [21] Y. Wu, S. Zhou, F. Qin, X. Ye, K. Zheng, Mathematical Model Analysis of Fenton Oxidation of Landfill Leachate, *Waste Manag.* 31 (2011) 468–474.
- [22] H.S. Li, S.Q. Zhou, Y.B. Sun, J. Lv, Nitrogen and carbon removal from Fenton-treated leachate by denitrification and biofiltration, *Bioresour. Technol.* 101 (2010) 7736–7743.
- [23] J. Niu, Y. Li, E. Shang, Z. Xu, J. Liu, Electrochemical oxidation of perfluorinated compounds in water, *Chemosphere* 146 (2016) 526–538.
- [24] H. Shi, Y. Wang, C. Li, R. Pierce, S. Gao, Q. Huang, Degradation of perfluorooctanesulfonate by reactive electrochemical membrane composed of magneli phase titanium suboxide, *Environ. Sci. Technol.* 53 (2019) 14528–14537.
- [25] T.X.H. Le, H. Haflich, A.D. Shah, B.P. Chaplin, Energy-efficient electrochemical oxidation of perfluoroalkyl substances using a Ti_4O_7 reactive electrochemical membrane anode, *Environ. Sci. Technol. Lett.* 6 (2019) 504–510.
- [26] S. Pei, C. Shen, C. Zhang, N. Ren, S. You, Characterization of the interfacial joule heating effect in the electrochemical advanced oxidation process, *Environ. Sci. Technol. Lett.* 5 (2019) 4406–4415.
- [27] H. Song, L. Yan, J. Jiang, J. Ma, Z. Zhang, J. Zhang, P. Liu, T. Yang, Electrochemical activation of persulfates at BDD anode: Radical or nonradical oxidation? *Water Res* 128 (2018) 393–401.
- [28] F. Wu, J. Nan, T. Wang, Z. Ge, B. Liu, M. Chen, X. Ye, Highly selective electrosynthesis of H_2O_2 by N, O co-doped graphite nanosheets for efficient electro-Fenton degradation of p-nitrophenol, *J. Hazard. Mater.* 446 (2023) 130733.
- [29] H. Guo, C. Zhao, H. Xu, H. Hao, Z. Yang, N. Li, W. Xu, Enhanced H_2O_2 formation and norfloxacin removal by electro-Fenton process using a surface-reconstructed graphite felt cathode: New insight into synergistic mechanism of defective active sites, *Environ. Res.* 220 (2023) 115221.
- [30] C. Wan, L. Zhao, C. Wu, L. Lin, X. Liu, Bi⁵⁺ doping improves the electrochemical properties of Ti/SnO₂-Sb/PbO₂ electrode and its electrocatalytic performance for phenol, *J. Clean. Prod.* 380 (2022) 135005.
- [31] Y. Zhang, C. Zhang, D. Shao, H. Xu, Y. Rao, G. Tan, W. Yan, Magnetically assembled electrodes based on Pt, RuO₂-IrO₂-TiO₂ and Sb-SnO₂ for electrochemical oxidation of wastewater featured by fluctuant Cl⁻ concentration, *J. Hazard. Mater.* 421 (2022) 126803.
- [32] X. Duan, Q. Wang, S. Tu, W. Wang, X. Sui, L. Chang, Electrocatalytic degradation of 2,4-dichlorophenol by a 3DG-PbO₂ powdered anode: experimental and theoretical insights, *Sep. Purif. Technol.* 282 (2022) 120003.
- [33] K. Wang, D. Huang, W. Wang, Y. Li, L. Xu, J. Li, Y. Zhu, J. Niu, Enhanced decomposition of long-chain perfluorocarboxylic acids (C9-C10) by electrochemical activation of peroxymonosulfate in aqueous solution, *Sci. Total Environ.* 758 (2021) 143666.
- [34] K. Wang, D. Huang, W. Wang, Y. Ji, J. Niu, Enhanced perfluorooctanoic acid degradation by electrochemical activation of peroxymonosulfate in aqueous solution, *Environ. Int.* 137 (2020) 105562.
- [35] W. Zeng, H. Zhang, R. Wu, L. Liu, G. Li, H. Liang, Environment-friendly and efficient electrochemical degradation of sulfamethoxazole using reduced TiO₂ nanotube arrays-based Ti membrane coated with Sb-SnO₂, *J. Hazard. Mater.* 446 (2022) 130642.
- [36] W. Sun, Y. Sun, K.J. Shah, H. Zheng, B. Ma, Electrochemical degradation of oxytetracycline by Ti-Sn-Sb/gamma-Al₂O₃ three-dimensional electrodes, *J. Environ. Manag.* 241 (2019) 22–31.
- [37] S. Man, X. Zeng, Z. Yin, H. Yang, H. Bao, K. Xu, L. Wang, X. Ge, Z. Mo, W. Yang, X. Li, Preparation of a novel Ce and Sb co-doped SnO₂ nanoflowers electrode by a two-step (hydrothermal and thermal decomposition) method for organic pollutants electrochemical degradation, *Electrochim. Acta* 411 (2022) 140066.
- [38] I.J. Peter, S. Vijaya, S. Anandan, P. Nithiananthi, Microwave synthesis and analysis of Sb₂S₃ nanostructures as IR photon-absorber and counter electrode for the design of symmetric solar cells, *Mater. Lett.* 276 (2020) 128160.
- [39] L. Žigas, A. Audžijonis, J. Grigas, Origin of weak ferroelectricity in semiconductive Sb₂S₃ crystal, *J. Phys. Chem. Sol. Ids.* 101 (2017) 5–9.
- [40] P. Ge, H. Hou, X. Ji, Z. Huang, S. Li, L. Huang, Enhanced stability of sodium storage exhibited by carbon coated Sb₂S₃ hollow spheres, *Mater. Chem. Phys.* 203 (2018) 185–192.
- [41] G. Wang, H. Zhang, W. Wang, X. Zhang, Y. Zuo, Y. Tang, X. Zhao, Fabrication of Fe-TiO₂-NTs/SnO₂-Sb-Ce electrode for electrochemical degradation of aniline, *Sep. Purif. Technol.* 268 (2021) 118591.
- [42] Q. Zhuo, J. Wang, J. Niu, B. Yang, Y. Yang, Electrochemical oxidation of perfluorooctane sulfonate (PFOS) substitute by modified boron doped diamond (BDD) anodes, *Chem. Eng. J.* 379 (2020) 122280.
- [43] X. Duan, W. Wang, Q. Wang, X. Sui, N. Li, L. Chang, Electrocatalytic degradation of perfluorooctane sulfonate (PFOS) on a 3D graphene-lead dioxide (3DG-PbO₂) composite anode: Electrode characterization, degradation mechanism and toxicity, *Chemosphere* 260 (2020) 127587.
- [44] F. Ghanbari, M. Moradi, Application of peroxymonosulfate and its activation methods for degradation of environmental organic pollutants: Review, *Chem. Eng. J.* 310 (2017) 41–62.
- [45] Y. Zhang, X. Chen, C. Liang, L. Yin, Y. Yang, Reconstructing the coordination environment of single atomic Fe-catalysts for boosting the Fenton-like degradation activities, *Appl. Catal. B Environ.* 315 (2022) 121536.

- [46] Y. Long, Z. Cao, W. Wu, W. Liu, P. Yang, X. Zhan, R. Chen, D. Liu, W. Huang, Rational modulation of Fe single-atom electronic structure in a Fe-N₂B₄ configuration for preferential ¹O₂ generation in Fenton-like reactions, *Appl. Catal. B Environ.* 344 (2024) 123643.
- [47] C. Ricca, F. Labat, C. Zavala, N. Russo, C. Adamo, G. Merino, E. Sicilia, B. N-Codoped graphene as catalyst for the oxygen reduction reaction: Insights from periodic and cluster DFT calculations, *J. Comput. Chem.* 39 (2018) 637–647.
- [48] J. Aihara, Reduced HOMO-LUMO gap as an index of kinetic stability for polycyclic aromatic hydrocarbons, *J. Phys. Chem. A* 103 (1999) 7487–7495.
- [49] C. Dang, F. Sun, H. Jiang, T. Huang, W. Liu, X. Chen, H. Ji, Pre-accumulation and in-situ destruction of diclofenac by photo-regenerable activated carbon fiber supported titanate nanotubes composite material: Intermediates, DFT calculation, and ecotoxicity, *J. Hazard. Mater.* 400 (2020) 123225.
- [50] M. Frisch, G. Trucks, H.B. Schlegel, G.E. Scuseria, M.A. Robb, J.R. Cheeseman, G. Scalmani, V. Barone, B. Mennucci, G. Petersson, Gaussian 09, Revision D. 01., 201, Gaussian, Inc., Wallingford CT, 2009.
- [51] T. Lu, F.M. Chen, Multiwfn: A Multifunctional Wavefunction Analyzer, *J. Comput. Chem.* 33 (2012) 580–592.
- [52] T. Lu, S. Manzetti, Wavefunction and reactivity study of benzo[al]pyrene diol epoxide and its enantiomeric forms, *Struct. Chem.* 25 (2014) 1521–1533.
- [53] I.J. Peter, S. Vijaya, S. Anandan, P. Nithiananthi, Sb2S3 entrenched MWCNT composite as a low-cost Pt-free counter electrode for dye-sensitized solar cell and a viewpoint for a photo-powered energy system, *Electrochim. Acta* 390 (2021) 138864.
- [54] T. Stamenković, N. Bundaleski, T. Barudžija, I. Validžić, V. Lojpur, XPS study of iodine and tin doped Sb2S3 nanostructures affected by non-uniform charging, *Appl. Surf. Sci.* 567 (2021) 150822.
- [55] A. Chen, S.V. Nair, B. Miljkovic, H.E. Ruda, Z. Ji, A DFT computational study of the mechanism of super-high oxygen evolution potential of W doped SnO₂ anodes, *J. Electroanal. Chem.* 855 (2019) 113499.
- [56] X. Chen, D. Vione, T. Borch, J. Wang, Y. Gao, Nano-MoO₂ activates peroxymonosulfate for the degradation of PAH derivatives, *Water Res* 192 (2021) 116834.
- [57] Y. Wu, Y. Wang, T. Pan, X. Yang, Oxidation of tetrabromobisphenol A (TBBPA) by peroxymonosulfate: The role of in-situ formed HOBr, *Water Res* 169 (2020) 115202.
- [58] M. Li, Y.-T. Jin, J.-F. Yan, Z. Liu, N.-X. Feng, W. Han, L.-W. Huang, Q.-K. Li, K.-L. Yeung, S.-Q. Zhou, C.-H. Mo, Exploration of perfluoroctane sulfonate degradation properties and mechanism via electron-transfer dominated radical process, *Water Res.* 215 (2022) 118259.
- [59] Z.Y. Guo, C.X. Li, M. Gao, X. Han, Y.J. Zhang, W.J. Zhang, W.W. Li, Mn-O Covalency Governs the Intrinsic Activity of Co-Mn Spinel Oxides for Boosted Peroxymonosulfate Activation, *Angew. Chem. Int. Ed.* 60 (2021) 274–280.
- [60] X. Duan, H. Sun, S. Wang, Metal-Free Carbocatalysis in Advanced Oxidation Reactions, *Acc. Chem. Res.* 51 (2018) 678–687.
- [61] J. Lu, R. Hou, Y. Wang, L. Zhou, Y. Yuan, Surfactant-sodium dodecyl sulfate enhanced degradation of polystyrene microplastics with an energy-saving electrochemical advanced oxidation process (EAOP) strategy, *Water Res* 226 (2022) 119277.
- [62] J. Luo, S. Bo, Y. Qin, Q. An, Z. Xiao, S. Zhai, Transforming goat manure into surface-loaded cobalt/biochar as PMS activator for highly efficient ciprofloxacin degradation, *Chem. Eng. J.* 395 (2020) 125063.
- [63] J. Zou, J. Ma, L. Chen, X. Li, Y. Guan, P. Xie, C. Pan, Rapid acceleration of ferrous iron/peroxymonosulfate oxidation of organic pollutants by promoting Fe(III)/Fe(II) cycle with hydroxylamine, *Environ. Sci. Technol.* 47 (2013) 11685–11691.
- [64] P. Gu, C. Zhang, Z. Sun, H. Zhang, Q. Zhou, S. Lin, J. Rong, M.R. Hoffmann, Enhanced photoreductive degradation of perfluoroctanesulfonate by UV irradiation in the presence of ethylenediaminetetraacetic acid, *Chem. Eng. J.* 379 (2020) 122338.
- [65] N. Duinslaeger, J. Radjenovic, Electrochemical degradation of per- and polyfluoroalkyl substances (PFAS) using low-cost graphene sponge electrodes, *Water Res.* 213 (2022) 118148.
- [66] C. Zhang, J. Tang, C. Peng, M. Jin, Degradation of perfluorinated compounds in wastewater treatment plant effluents by electrochemical oxidation with Nano-ZnO coated electrodes, *J. Mol. Liq.* 221 (2016) 1145–1150.
- [67] Y. Liu, X. Fan, X. Quan, Y. Fan, S. Chen, X. Zhao, Enhanced Perfluoroctanoic Acid Degradation by Electrochemical Activation of Sulfate Solution on B/N Codoped Diamond, *Environ. Sci. Technol.* 53 (2019) 5195–5201.
- [68] Q. Zhuo, J. Han, J. Niu, J. Zhang, Degradation of a persistent organic pollutant perfluoroctane sulphonate with Ti/SnO₂-Sb₂O₅/PbO₂-PTFE anode, *Emerg. Contam.* 6 (2020) 44–52.
- [69] M.J. Chen, S.L. Lo, Y.C. Lee, C.C. Huang, Photocatalytic decomposition of perfluoroctanoic acid by transition-metal modified titanium dioxide, *J. Hazard. Mater.* 288 (2015) 168–175.
- [70] C.B. Ong, A.W. Mohammad, L.Y. Ng, E. Mahmoudi, S. Azizkhani, N.H. Hayati Hairom, Solar photocatalytic and surface enhancement of ZnO/rGO nanocomposite: Degradation of perfluoroctanoic acid and dye, *Process Safe. Environ.* 112 (2017) 298–307.
- [71] Y. Yang, Z. Chen, H. Huang, Y. Liu, J. Zou, S. Shen, J. Yan, J. Zhang, Z. Zhuang, Z. Luo, C. Yang, Y. Yu, Z. Zou, Synergistic surface activation during photocatalysis on perovskite derivative sites in heterojunction, *Appl. Catal. B Environ.* 323 (2023) 122146.
- [72] H. Li, G. Liu, B. Zhou, Z. Deng, Y. Wang, L. Ma, Z. Yu, K. Zhou, Q. Wei, Periodic porous 3D boron-doped diamond electrode for enhanced perfluoroctanoic acid degradation, *Sep. Purif. Technol.* 297 (2022) 121556.
- [73] J.N. Uwayezu, I. Carabante, T. Lejon, P. van Hees, P. Karlsson, P. Hollman, J. Kumpiene, Electrochemical degradation of per- and poly-fluoroalkyl substances using boron-doped diamond electrodes, *J. Environ. Manag.* 290 (2021) 112573.
- [74] S. Barisci, R. Suri, Electrooxidation of short and long chain perfluorocarboxylic acids using boron doped diamond electrodes, *Chemosphere* 243 (2020) 125349.
- [75] S. Barisci, R. Suri, Electrooxidation of short- and long-chain perfluoroalkyl substances (PFASs) under different process conditions, *J. Environ. Chem. Eng.* 9 (2021) 105323.
- [76] Q. Wang, M. Liu, H. Zhao, Y. Chen, F. Xiao, W. Chu, G. Zhao, Efficiently degradation of perfluoroctanoic acid in synergic electrochemical process combining cathodic electro-Fenton and anodic oxidation, *Chem. Eng. J.* 378 (2019) 122071.